

# 1 **Integrated Triassic sediment routing along eastern** 2 **Gondwana (Australia)**

3 **Matthew Scipione<sup>1</sup>, Romain Vaucher<sup>1</sup>, Eric Roberts<sup>2</sup>, Alex J. McCoy-West<sup>1,5</sup>, Joan**  
4 **Esterle<sup>3</sup>, Ashten Turner<sup>1</sup> and Espen Knutsen<sup>1,4</sup>**

5 *<sup>1</sup> College of Science and Engineering , James Cook University, Townsville, Qld 4811, Australia*

6 *<sup>2</sup>Department of Geology and Geological Engineering, Colorado School of Mines, 1500 Illinois*  
7 *St, Golden, CO 80401, United States*

8 *<sup>3</sup>School of the Environment, The University of Queensland, Brisbane 4072, Australia*

9 *<sup>4</sup>Queensland Museum Tropics, Queensland Museum, Townsville, Queensland 4810, Australia*

10 *<sup>5</sup>Economic Geology Research Centre, James Cook University, Townsville, QLD, Australia*

11

12 **Correspondence:** Matthew Scipione (matt.scipione@my.jcu.edu.au)

13

## 14 **ORCID number**

15 Matthew Scipione: 0009-0000-7282-7419

16 Romain Vaucher: 0000-0003-3051-4128

17 Eric Roberts: 0000-0002-8583-7437

18 Alex McCoy-West: 0000-0003-4171-9276

19 Joan Esterle: 0000-0003-0775-5169

20 Espen Knutsen: 0000-0003-2646-2214

21 **Keywords:** detrital zircon, provenance, sediment routing, Bowen Basin, Triassic, Gondwana

22

23

24 **Abstract**

25 Triassic continental sedimentary basins along the eastern margin of Gondwana record drainage  
26 reorganisation and sediment routing, but provenance links among adjacent basins remain  
27 uncertain. This study integrates detrital zircon U–Pb data and sandstone petrography from the  
28 Triassic Rewan Group and Clematis Group of the northern Bowen Basin with published  
29 palaeocurrent constraints and compares these with published Triassic detrital zircon datasets  
30 from the Galilee Basin and the Gympie Terrane. Rewan Group zircon spectra are dominated  
31 by Middle Triassic grains (ca. 245 Ma) with persistent Carboniferous components. Sagittarius  
32 Sandstone and Arcadia Formation samples plot close together in a multidimensional scaling  
33 ordination of Wasserstein-2 distances, indicating similar age mixtures across the sampled  
34 Rewan Group depocentres. Short crystallisation-to-deposition age gaps and feldspar-poor,  
35 lithic-rich petrography are consistent with sustained volcanoclastic input from the eastern  
36 Tasmanide margin during Rewan Group deposition. Clematis Group spectra are more variable,  
37 contain fewer Triassic zircons, and include a larger proportion of grains older than ca. 400 Ma.  
38 More quartzose petrography and longer crystallisation-to-deposition age gaps suggest greater  
39 continental-interior input and/or increased recycling during later Triassic deposition. Regional  
40 comparisons place Rewan Group samples with the Bandanna Formation and Gympie Terrane  
41 units, whereas Clematis Group samples are closer to the Warang Sandstone and Porcupine  
42 Gorge Formation. Moolayember Formation reference spectra shift back towards a Rewan  
43 Group-like signal, suggesting that the Clematis Group provenance shift may have been  
44 temporally limited. These results provide a quantitative basis for testing basin connectivity and  
45 for linking changes in provenance to sediment routing within retroarc foreland systems.

46

## 47 **Highlights**

- 48 • Integrated provenance data help test sediment-routing change in retroarc basin  
49 systems.
- 50 • Rewan Group spectra record sustained sediment supply from an active continental  
51 margin.
- 52 • Clematis Group sandstones show increased inland and recycled sediment  
53 contributions.
- 54 • Regional comparisons identify source links among neighbouring eastern Australian  
55 basins.
- 56 • Results help explain how drainage networks reorganise in retroarc basin systems.

57

## 58 **Introduction**

59 Detrital zircon U–Pb geochronology is widely used to evaluate provenance and basin-  
60 scale sediment routing. Zircon is resilient to weathering and recycling, and age distributions  
61 can be compared quantitatively among stratigraphic levels and depositional systems (Adams  
62 et al., 2022; Andrade et al., 2023; Dickinson & Gehrels, 2009; Foley et al., 2021; Henderson  
63 & Fergusson, 2019; Li et al., 2015; Phillips et al., 2018; Romans et al., 2016; Rosenbaum et  
64 al., 2020; Shaanan et al., 2018; Shaanan & Rosenbaum, 2018; Sobczak et al., 2022; Todd,  
65 2020; Tucker et al., 2013). In systems with multiple sediment sources, differences in zircon  
66 age spectra can result from shifts in source input, transport pathways, mixing, or recycling. To  
67 interpret these differences, datasets must be filtered consistently and compared using  
68 distribution-based similarity metrics. Detrital zircon data can also constrain maximum  
69 depositional ages when young grains are present, providing internal chronostratigraphic  
70 markers for correlation within and between depocentres (Foley et al., 2020, 2021; Tucker et

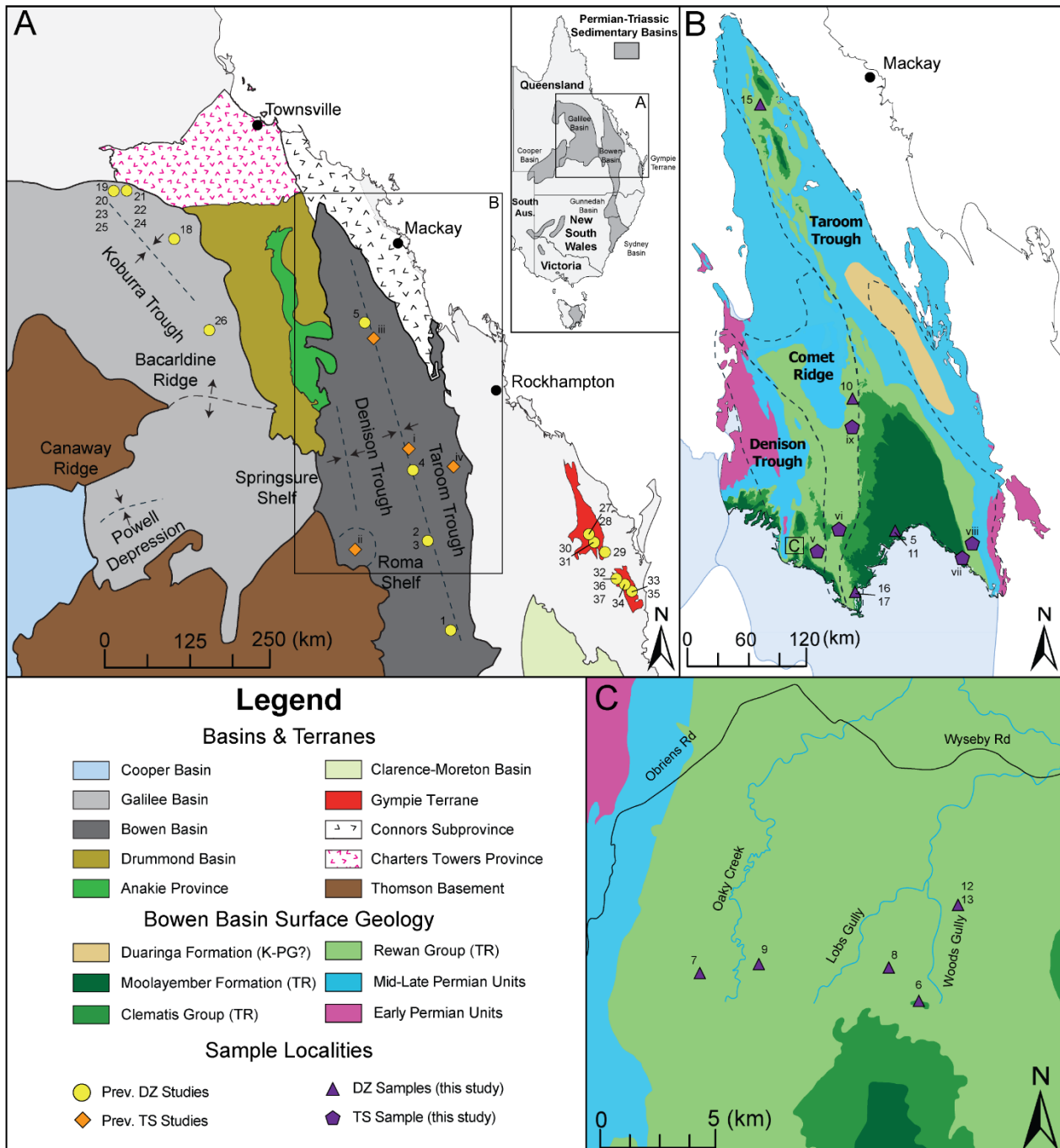
71 al., 2016). This is particularly relevant to the Triassic of eastern Australia, when Late Permian–  
72 Triassic deformation reorganised drainage and altered sediment routing.

73 Eastern Australia includes retroarc basins adjacent to the Tasmanides, an accretionary  
74 orogenic belt along the eastern margin of Gondwana (Figure 1). Late Permian to Triassic  
75 shortening during the Hunter–Bowen Orogeny affected subsidence and relief across this  
76 system, which likely influenced drainage and sediment routing (Hoy, 2020; P.F. Li et al., 2012;  
77 Rosenbaum et al., 2020). The northern Bowen Basin (Figure 1) preserves Triassic fluvial to  
78 floodplain successions across multiple structural domains. It includes packages that can be used  
79 to test shifts between margin-derived detritus and cratonward or recycled sources. A key gap  
80 is that Triassic provenance links between the Bowen Basin, Galilee Basin, and Gympie Terrane  
81 remain uncertain (Figure 1). Existing detrital zircon datasets have uneven stratigraphic  
82 coverage and are often processed and reported using different conventions. This limits direct,  
83 quantitative comparison among basins and terranes. This study targets Triassic sandstones from  
84 the Rewan Group (Sagittarius Sandstone and Arcadia Formation) and the Clematis Group  
85 (Figure 2). These units span an interval in which sediment supply may have shifted from mainly  
86 margin-derived, arc-proximal sources to a more mixed signal with greater craton-derived and  
87 recycled input. Sandstone petrography and quartz–feldspar–lithic (QFL) point counts provide  
88 independent compositional context and help link zircon age populations to source lithologies  
89 and sediment dispersal pathways, but they do not uniquely resolve terrane-scale mixing,  
90 recycling, or basin-to-basin sediment transfer (Bashari, 2000; Grech, 2001; Kassan, 1994;  
91 Michaelsen & Henderson, 2000).

92 Published detrital zircon datasets provide useful regional reference points, but uneven  
93 coverage and differing workflows limit direct comparison. Gympie Terrane datasets provide  
94 an arc-proximal reference (Li et al., 2015; Rosenbaum et al., 2020), whereas Galilee Basin  
95 datasets provide a cratonward comparator and include signals of recycled basin fill (Phillips et

96 al., 2018). Recycling and sediment transfer between basins can obscure source interpretations,  
97 so consistent methods and direct inter-basin comparison are required (Adams et al., 2022;  
98 Sobczak et al., 2022). These datasets define regional endmembers, but the northern Bowen  
99 Basin still lacks stratigraphically constrained, multi-proxy provenance data that can be directly  
100 compared with adjacent basins.

101         New stratigraphically constrained detrital zircon U–Pb data from Triassic sandstones  
102 in the northern Bowen Basin are integrated with sandstone petrography. Using the revised  
103 Rewan Group chronostratigraphy of Scipione et al. (2026), the analysis tests whether  
104 provenance shifts through the Rewan and Clematis groups reflect changes in source terranes,  
105 sediment-routing integration, or recycling.



106 **Figure 1.** (A) Regional map of Permian–Triassic basins and terranes in eastern Queensland,  
 107 Australia, showing the locations of published detrital zircon (DZ) datasets compiled for  
 108 regional comparison. Thin-section data are denoted by *i* = Kassan (1994), *ii* = Bashari (2000),  
 109 *iii* = Michaelsen and Henderson (2000), and *iv* = Grech (2001). (B) Northern Bowen Basin  
 110 map showing major structural elements (Taroom Trough, Denison Trough, and Comet Ridge)  
 111 and the surface distribution of key stratigraphic packages. Symbols show sample localities for  
 112 this study, including DZ samples and thin-section (TS) samples, together with locations from  
 113 previous DZ and petrographic studies. Wells sampled for thin section in this study are denoted  
 114 by *v* = Taroom 8, *vi* = Huntly 1, *vii* = Taroom 13, *viii* = Theodore NS150, and *ix* = Blackdown  
 115 3. (C) Enlarged inset of the Rewan area. Numbered labels adjacent to symbols identify  
 116 individual sample localities and correspond to the sample numbering used in the Table 3.  
 117 Symbols distinguish DZ and thin-section (TS) samples from this study and from previous  
 118 studies.

## 119 **2. Geological background**

120

### 121 **2.1 Regional geology**

122         The Bowen Basin lies within the Tasmanides of eastern Australia, an accretionary  
123 orogenic system that developed along the eastern Gondwanan margin through long-lived  
124 convergent-margin processes (Asmussen et al., 2023; Collins, 1991; Glen, 2005; Jessop et al.,  
125 2019; Rosenbaum et al., 2025). The Bowen–Gunnedah–Sydney Basin system extends from  
126 Townsville to Sydney (Figure 1). It records a transition from Early Permian extension to Late  
127 Permian–Triassic shortening and foreland-basin development during the Hunter–Bowen  
128 Orogeny and its post-orogenic adjustment (Brakel et al., 2009; Green et al., 1997; Jell, 2013;  
129 Korsch, Totterdell, Cathro, et al., 2009). During the Late Permian–Triassic interval, the  
130 deformation propagated into the basin and reorganised accommodation and relief, providing  
131 conditions for rapid changes in sediment routing, catchment, and recycling pathways  
132 (Babaahmadi et al., 2017; Campbell et al., 2017; Hoy, 2020; Hoy et al., 2018). The study area  
133 in the northern Bowen Basin, Queensland, lies close to the coastal part of the orogen and along  
134 potential pathways for craton-derived sediment (Figure 1A), providing a strong position to  
135 evaluate competing provenance models using stratigraphically constrained detrital zircon (DZ)  
136 data.

137         From a provenance perspective, the main potential sediment sources are the New  
138 England Orogen (NEO) and related arc terranes near the former plate margin, and the more  
139 inland Thomson Orogen and associated basement provinces that underlie and border the  
140 foreland basin (Baker, 1997; Glen, 2005; Jessop et al., 2019; Sobczak et al., 2022). The NEO  
141 is a composite system of accreted terranes and magmatic belts and is commonly treated as the  
142 main eastern sediment source for Permian–Triassic basins in Queensland (Collins, 1991; P.F.  
143 Li et al., 2012; Rosenbaum et al., 2025; Siegel et al., 2020). Continued convergence, rollback,

144 and arc reconfiguration into the Triassic provide a mechanism for sustained delivery of near-  
145 contemporaneous zircon to adjacent depocentres, either by direct erosion of arc and plutonic  
146 sources or by recycling of volcanoclastic successions (Campbell et al., 2022; Jessop et al., 2019;  
147 Li et al., 2015; Rosenbaum, 2026; Sliwa et al., 2018). If the NEO dominated sediment supply,  
148 Triassic DZ spectra would be expected to be rich in Late Palaeozoic–Triassic ages, with  
149 secondary Devonian–Carboniferous and older Palaeozoic components derived either from  
150 Tasmanide basement or recycled basin fill (Foley et al., 2021; Todd et al., 2022; Tucker et al.,  
151 2016).

152  
153 **Figure 2.** *Composite stratigraphic columns show major lithostratigraphic units plotted against*  
154 *age and palynological zonation, with broad depositional environments indicated by colour.*  
155 *Symbols mark detrital zircon (DZ) maximum depositional ages from this study and previously*  
156 *published DZ ages from the Galilee Basin and Gympie Terrane datasets used for regional*  
157 *comparison.*

158 The Thomson Orogen underlies the Bowen–Galilee region and is locally exposed in  
159 basement inliers such as the Anakie Inlier and Charters Towers Province (Figure 1A; Jell,  
160 2013). Thomson-related DZ spectra commonly include Neoproterozoic–Cambrian and  
161 Mesoproterozoic Grenvillian populations, although these overlap with other Tasmanide  
162 sources (Asmussen, 2020; Purdy et al., 2016; Sobczak et al., 2022; Spampinato et al., 2015).  
163 These cratonward modes could enter Triassic foreland strata through western catchments,  
164 recycling of older sedimentary rocks, or along-basin transport between depocentres (Korsch,  
165 Totterdell, Fomin, et al., 2009; Sobczak et al., 2022).

166 The Galilee Basin (Figure 1A) provides the main cratonward comparison because it lies  
167 adjacent to the Bowen Basin and overlies Thomson Orogen crustal domains that could have  
168 supplied sediment from the west or northwest to Triassic successions (Phillips et al., 2018;  
169 Todd, 2020; Todd et al., 2022; Van Heeswijck, 2010, 2018). Published DZ datasets from the  
170 basin record mixed age populations that include both cratonward basement signatures and  
171 Tasmanide margin components and thus provide a practical regional comparator (Phillips et

172 al., 2018; Todd et al., 2022). At the active-margin side of the foreland system, the Gympie  
173 Terrane provides the arc-proximal benchmark for Triassic detrital zircon age populations (Li et  
174 al., 2015; Rosenbaum et al., 2020).

175

## 176 **2.2 Bowen Basin framework and stratigraphy**

177 The Triassic succession of the northern Bowen Basin is underlain by the upper Permian  
178 Blackwater Group, which forms the underlying unit and an important reference for provenance  
179 analysis (Figure 2). Within the Blackwater Group, the Bandanna Formation and related coal  
180 measures comprise alternating marine mudstones, coal-rich intervals, and fluvial sandstones  
181 that record repeated shifts in accommodation and shoreline position during late Permian  
182 foreland basin fill (Fielding et al., 2022; Naher et al., 2025; Phillips et al., 2017, 2018). These  
183 upper Permian units are relevant to Triassic provenance because they include regionally  
184 traceable volcanic ash beds that provide age anchors close to the Permian–Triassic transition  
185 (Ayaz et al., 2016; Brakel et al., 2009; Grech, 2001; Green et al., 1997; Korsch, Totterdell,  
186 Fomin, et al., 2009; McKellar et al., 2015; Scipione et al., 2026).

187 Continental red-bed deposition of the Rewan Group marks a major shift in depositional  
188 style following the cessation of coal accumulation and the associated wetland environments in  
189 the latest Permian succession (Fielding et al., 1997; Grech, 2001; Jensen, 1975; Lang et al.,  
190 2001). The basal Triassic surface is commonly expressed as an erosional contact, but the  
191 stratigraphic expression and duration of missing section vary across structural domains (Exon,  
192 1976; Grech, 2001; Green et al., 1997). New chronostratigraphic constraints indicate that the  
193 contact is time transgressive and that preservation differs between the foredeep and the  
194 backbulge at the scale of the northern basin (Scipione et al., 2026). In the Taroom Trough  
195 foredeep, depositional ages and maximum depositional ages from the lowermost Triassic red  
196 beds show progressive younging above the latest Permian deposits, consistent with relatively

197 continuous accommodation and sedimentation through the Early and Middle Triassic at the  
198 resolution of the detrital record (Scipione et al., 2026). In contrast, the Denison Trough  
199 (backbulge) preserves a condensed Triassic record above the latest Permian horizons,  
200 suggesting a substantial interval of non-deposition and/or erosion across the Permian-Triassic  
201 transition (Scipione et al., 2026). This spatial contrast is central to the provenance framework  
202 because it influences both the completeness of the stratigraphic archive and the likelihood that  
203 older successions were exposed for recycling during early Triassic basin evolution.

204         The Sagittarius Sandstone forms the basal fluvial package of the Rewan Group and  
205 records the earliest preserved phase of continental drainage development within the Triassic  
206 succession (Figure 2). It is typically composed of fine- to medium-grained channel sandstones  
207 with trough cross-bedding, ripple lamination, and scour surfaces, interbedded with thick red  
208 siltstone and mudstone floodplain deposits (Exon, 1976; Grech, 2001; Green et al., 1997;  
209 Jensen, 1975; Lang et al., 2001). The basal surface of the Sagittarius Sandstone is commonly  
210 treated as a sequence boundary associated with regional base-level fall and incision at the  
211 Permian–Triassic transition, but its expression varies between structural domains and may be  
212 time transgressive at the scale of the northern basin (Brakel et al., 2009; Grech, 2001; Scipione  
213 et al., 2026). The overlying Arcadia Formation comprises a several hundred metres thick  
214 succession of fluvial channel and overbank deposits that grades upward into mud-rich  
215 floodplain intervals with palaeosols and pedogenic carbonate, consistent with prolonged  
216 floodplain aggradation under arid to semiarid conditions (Brakel et al., 2009; Exon, 1976;  
217 Grech, 2001; Jensen, 1975; Lang et al., 2001). Within the Arcadia Formation, coarse-grained  
218 sandstone bodies such as the Brumby Sandstone Member have been interpreted as channelised  
219 packages that record changes in accommodation and sediment supply within broader Rewan  
220 Group evolution (Grech, 2001; Lang et al., 2001). Rewan Group sandstones are also  
221 characterised by abundant volcanoclastic detritus, consistent with strong sediment supply from

222 the NEO and contemporaneous magmatic activity along the active margin (Bashari, 2000;  
223 Michaelsen & Henderson, 2000).

224 A further basin-scale change occurs at the base of the Clematis Group, where quartz-  
225 rich, commonly pebbly sandstones rest sharply on Rewan Group red beds in many parts of the  
226 basin (Brakel et al., 2009; Jensen, 1975; Kassan, 1994). Clematis Group deposits are more  
227 texturally and compositionally mature than the underlying Rewan Group and have been linked  
228 to changing sediment supply and drainage during waning Hunter–Bowen deformation,  
229 although longer transport, storage, and recycling may also have amplified the signal (Baker,  
230 1997; Brakel et al., 2009; Grech, 2001; Kassan, 1994; Korsch, Totterdell, Fomin, et al., 2009;  
231 Michaelsen & Henderson, 2000). The Moolayember Formation caps the Triassic succession  
232 and includes a laterally persistent basal flooding interval, but the extent and mechanism of any  
233 marine influence remain uncertain (Brakel et al., 2009; Grech, 2001; Green et al., 1997).  
234 Together, the Bandanna Formation and overlying Triassic units provide the framework for  
235 testing whether provenance signals track margin-derived volcanoclastic supply during Rewan  
236 Group deposition and whether more mature, cratonward-derived sediment became more  
237 important during Clematis Group and younger Triassic deposition (Figure 2).

238

### 239 **2.3 Previous detrital zircon U–Pb geochronology**

240 Regional detrital zircon U–Pb datasets provide the basis for comparing Triassic  
241 sediment routing among eastern Australian basins. Gympie Terrane datasets provide an arc-  
242 proximal reference, Galilee Basin datasets provide a cratonward reference, and Bowen Basin  
243 system datasets provide broader context for provenance mixing and sediment redistribution  
244 (Adams et al., 2022; Li et al., 2015; Phillips et al., 2018; Sobczak et al., 2022; Todd et al.,  
245 2022). The geographic and stratigraphic relationships of these datasets are summarised in  
246 Figures 1 and 2.

247 Detrital zircon spectra are not unique fingerprints, so zircon ages are interpreted  
248 alongside independent provenance and transport constraints. Recent studies have expanded  
249 regional DZ coverage and improved stratigraphic frameworks in adjacent basins, but a Triassic  
250 provenance synthesis for the northern Bowen Basin is still lacking (Adams et al., 2022;  
251 Sobczak et al., 2022). The regional comparison is used to identify broad provenance patterns  
252 rather than exact sample-to-sample equivalence, because sampling density, analytical  
253 workflow, and stratigraphic correlation vary among studies (Andrade et al., 2023; Li et al.,  
254 2015; Phillips et al., 2018; Todd et al., 2022).

255 Accordingly, published Triassic datasets from the Galilee Basin and Gympie Terrane  
256 (Adams et al., 2022; Li et al., 2015; Phillips et al., 2018; Rosenbaum et al., 2020; Sobczak et  
257 al., 2022; Todd et al., 2022) are compiled, reprocessed using a single filtering and reporting  
258 workflow, and compared directly with new stratigraphically constrained Triassic detrital zircon  
259 data from the northern Bowen Basin. This framework tests whether provenance patterns reflect  
260 persistent arc-dominated supply, increased continental interior contribution, or recycling  
261 driven mixing. It also tests whether basin-to-basin similarities reflect shared source access  
262 rather than coincidence.

263

### 264 **3. Methods**

265

#### 266 **3.1 Sampling strategy and sample context**

267 Detrital zircon samples were collected from outcrop and archived drill core across the  
268 northern Bowen Basin, Queensland (Figure 1B, C). Petrographic sampling focused on core  
269 intervals where continuous stratigraphic control is available. Surface exposures were combined  
270 with subsurface control from multiple wells to capture provenance variability along strike and  
271 across structural domains. Archived drill core was accessed through the Geological Survey of

272 Queensland core library in Brisbane. Sampling targeted biotite-rich sandstone to maximise  
273 zircon recovery and improve recovery of the youngest detrital component for MDA estimation.  
274 Typical outcrop sample mass was 1–5 kg, and core samples were taken over half-core intervals  
275 of approximately 15 cm.

276 The DZ dataset includes outcrop samples from the Arcadia Formation and basal  
277 Clematis Group. Arcadia Formation sandstones were sampled at Early Storms Creek, The  
278 Crater, Oaky Creek (Early Storms Station), and Duckworth Creek (Figure 1B, C). A Clematis  
279 Group sandstone was collected at Mount Round (Figure 1C) to provide an upper stratigraphic  
280 comparison to the Rewan Group interval. Core-based DZ sampling provides stratigraphic  
281 control through key intervals and extends coverage across depocentres in the northern Bowen  
282 Basin (Figure 1B). Core samples were collected from Rewan 1, Brumby Plains 1, Taroom 14,  
283 Drake NS27, and Theodore NS150 (Figure 1B, C).

284 Petrographic thin sections were prepared from a targeted subset of samples to provide  
285 compositional context for the DZ-based provenance interpretation and to support QFL  
286 classification. Representative photomicrographs include Bandanna Formation, Sagittarius  
287 Sandstone, Arcadia Formation, and Clematis Group samples from Taroom 8, Drake NS27,  
288 Blackdown 3, Huntly 1, Theodore NS150, Taroom 14, and Taroom 13. These include both DZ-  
289 analysed intervals and additional intervals used to broaden petrographic coverage.

290

### 291 **3.2 Sandstone Petrography**

292 Sandstone petrography was undertaken on 35 thin sections prepared from core samples  
293 across the northern Bowen Basin study area (Figure 1). The thin sections span the Bandanna  
294 Formation, Sagittarius Sandstone, Arcadia Formation, and Clematis Group (Figures 2, 3; Table  
295 1). Selected photomicrographs are presented in Figures 4 and 5 to illustrate key grain types,  
296 textures, and diagenetic features observed within each stratigraphic package.

297 Framework composition was quantified using QFL (quartz, feldspar, lithic fragments)  
298 point counting following the Gazzi-Dickinson approach (Dickinson & Suczek, 1979; Ingersoll  
299 et al., 1984). Each thin section was point counted on a systematic grid, with a target of ~300  
300 points per section. Framework grains, matrix, and pore space/diagenetic components were  
301 recorded separately to allow reproducible comparison among stratigraphic units. Counts were  
302 assigned to quartz, feldspar, lithic fragments, and matrix. Porosity, accessory minerals,  
303 authigenic minerals, and cements were excluded from the framework tally. Matrix was  
304 recorded during point counting but excluded from the QFL framework normalisation, so that  
305 plotted compositions represent only QFL (Figure 3).

306 Sandstone compositions were interpreted using the QFL classification of Garzanti  
307 (2016, 2019) and the provenance fields of Dickinson and Suczek (1979) and Dickinson et al.  
308 (1983). These plots are used to provide first order constraints on sediment character and source  
309 type and to complement detrital zircon provenance interpretations, rather than as a unique  
310 indicator of tectonic setting (Figures 4, 5).

311

### 312 **3.3 Detrital zircon U–Pb geochronology**

313 Samples were crushed and milled, and the <500 µm fraction was retained for mineral  
314 separation. Heavy mineral concentrates were produced using standard density and hydraulic  
315 methods, including Wilfley table concentration followed by heavy liquid separation (LMT;  
316 density 2.87). Zircons were handpicked under a binocular microscope. Approximately 300  
317 grains per sandstone sample were mounted in epoxy, polished to expose grain midsections, and  
318 carbon coated. Zircons were imaged by a Hitachi SU5000 scanning electron microscope with  
319 a cathodoluminescence filter (SEM-CL) to document internal zoning and to guide placement  
320 of ablation pits away from cracks, inclusions, and mixed domains.

321 U–Pb analyses were conducted at the Advanced Analytical Centre (AAC), James Cook  
322 University (JCU), Townsville, Australia, using a 193 nm ArF excimer laser coupled to an  
323 Agilent 8900 ICP–MS. Analyses used a 20  $\mu\text{m}$  spot diameter at 10 Hz, with fluence maintained  
324 at 5–10 J/cm<sup>2</sup>. Each analysis comprised a gas blank followed by 30–45 s of ablation. Primary  
325 and secondary zircon reference materials (GJ-1 and Temora-2) were analysed throughout each  
326 session to calibrate and monitor accuracy, bracketing groups of unknowns, and NIST 610 glass  
327 was used to monitor instrument behaviour and stability through time.

328 Data reduction was completed using Iolite/VizualAge following standard workflows  
329 for background subtraction, downhole fractionation correction, and drift correction (Paton et  
330 al., 2011). Analyses were screened for unstable signals and mixed-domain behaviour.  
331 Uncertainties are reported at  $2\sigma$  and include propagated external uncertainties based on session  
332 standards. Discordance was assessed using  $^{206}\text{Pb}/^{238}\text{U}$  and  $^{207}\text{Pb}/^{235}\text{U}$  systematics. Unless stated  
333 otherwise, detrital zircon analyses with >10% discordance were excluded from age spectra,  
334 Wasserstein-2 dissimilarity calculations, and maximum depositional age estimates. For grains  
335 younger than *ca.* 1500 Ma,  $^{206}\text{Pb}/^{238}\text{U}$  ages were used; for older grains,  $^{207}\text{Pb}/^{206}\text{Pb}$  ages were  
336 used.

337

### 338 **3.4 Statistical and graphical workflow**

339 Age spectra were visualised using kernel density estimates (KDEs) and cumulative  
340 distribution functions (CDFs). KDEs were used to show multimodal structure without binning  
341 artefacts, whereas CDFs were used for quantitative comparisons because they preserve the  
342 empirical rank structure of the data (Vermeesch, 2012). KDE shape depends on bandwidth and  
343 kernel choice, so KDEs are used here only as a qualitative visual aid. Quantitative comparisons  
344 are based on CDF-derived statistics from the filtered dataset. For the formation-level  
345 composites shown in Figure 6, concordant analyses were also grouped into broad regional age-

346 population bins to calculate the percentage contribution of each interval (Table 2). These  
347 percentages are used as summary descriptors of relative age-population abundance and do not  
348 replace the distribution-based comparisons (Figure 6, 7, 8).

349         Between-sample similarity was assessed using distance-based methods and ordination.  
350 Pairwise dissimilarity was quantified using the Wasserstein-2 distance calculated from  
351 empirical CDF, and the results were visualised using multidimensional scaling (MDS)  
352 (Vermeesch, 2018; Lipp & Vermeesch, 2022). The Wasserstein-2 distance measures the  
353 amount of distributional shift required to transform one age distribution into another. MDS  
354 projects the resulting pairwise distance matrix into two dimensions. Samples that plot close  
355 together therefore have similar overall age distributions, whereas samples that plot farther apart  
356 are more dissimilar. Dim 1 and Dim 2 are unitless ordination axes. No direct geological  
357 meaning is assigned to the axes themselves. Instead, the ordination is interpreted by comparison  
358 with the KDEs and other provenance constraints. To evaluate source-to-sink implications  
359 through time, crystallisation-to-deposition age-gap plots were used to compare zircon  
360 crystallisation ages with depositional constraints (Cawood et al., 2012). These plots are used  
361 here as interpretive context for provenance, not as stand-alone tectonic discriminants (Figure  
362 7).

363         Maximum depositional ages (MDA) were calculated to provide internal depositional  
364 constraints for stratigraphic comparison and for lag-time calculations. MDA were estimated  
365 using multiple approaches that capture different assumptions about the youngest population:  
366 (i) the youngest single grain (YSG), (ii) the youngest grain cluster (YGC), and (iii) a maximum  
367 likelihood age (MLA) estimate (Table 3; Vermeesch, 2021). MDA were calculated from <10%  
368 discordant analyses and were only treated as meaningful where the youngest population forms  
369 a coherent cluster of overlapping ages and where results are consistent with stratigraphic order  
370 (Coutts et al., 2019; Dickinson & Gehrels, 2009).

371

### 372 **3.5 Compilation and standardisation of published detrital zircon datasets**

373 Published detrital zircon datasets from surrounding basins and terranes were compiled  
374 from supplementary material to place the northern Bowen Basin results in a regional  
375 framework. The compiled datasets include Triassic and closely adjacent successions from the  
376 Galilee Basin (Phillips et al., 2018; Todd, 2020; Todd et al., 2022), the Gympie Terrane (Li et  
377 al., 2015; Rosenbaum et al., 2020) (Figure 1A), and the Surat Basin, including Triassic  
378 Moolayember Formation samples used for comparison (Figure 9) (Sobczak et al., 2022).  
379 Additional Triassic samples from adjacent basins and terranes were taken from the regional  
380 compilation of Adams et al. (2022).

381 Only studies that provide grain-scale ages (or equivalent downloadable tables) were  
382 included. Where raw ages and uncertainties were available, datasets were re-filtered using a  
383 consistent <10% discordance threshold and the same age-selection rules applied to the new  
384 data. Where only pre-filtered concordant datasets were published, the original filtering criteria  
385 were retained and documented (Table 3). Published comparison datasets therefore vary in  
386 concordant grain count and, in some cases, in original analytical and filtering workflow.  
387 Accordingly, the regional comparison emphasises broad and reproducible similarity structure  
388 rather than exact equivalence among all published spectra.

389

### 390 **3.6 Palaeocurrent**

391 Palaeocurrent data used in this study were compiled from published measurements  
392 rather than collected as part of this work. The compiled dataset includes palaeocurrent  
393 indicators reported for Triassic strata in the northern Bowen Basin and is used to provide  
394 independent constraints on sediment transport directions for the palaeodrainage reconstructions  
395 and routing interpretations. Palaeocurrent vectors shown in Figure 10 are taken from Jensen

396 (1975), Kassan (1994), and Grech (2001). Palaeocurrent measurements are plotted as reported  
397 in the original sources; where the original studies indicate structural (tilt) correction, their  
398 corrected orientations are retained, and where correction status is unclear, the vectors are  
399 treated as qualitative indicators of transport direction rather than definitive directional  
400 information.

401

## 402 **4. Results**

### 403 **4.1 Petrography and QFL compilation results relevant to provenance**

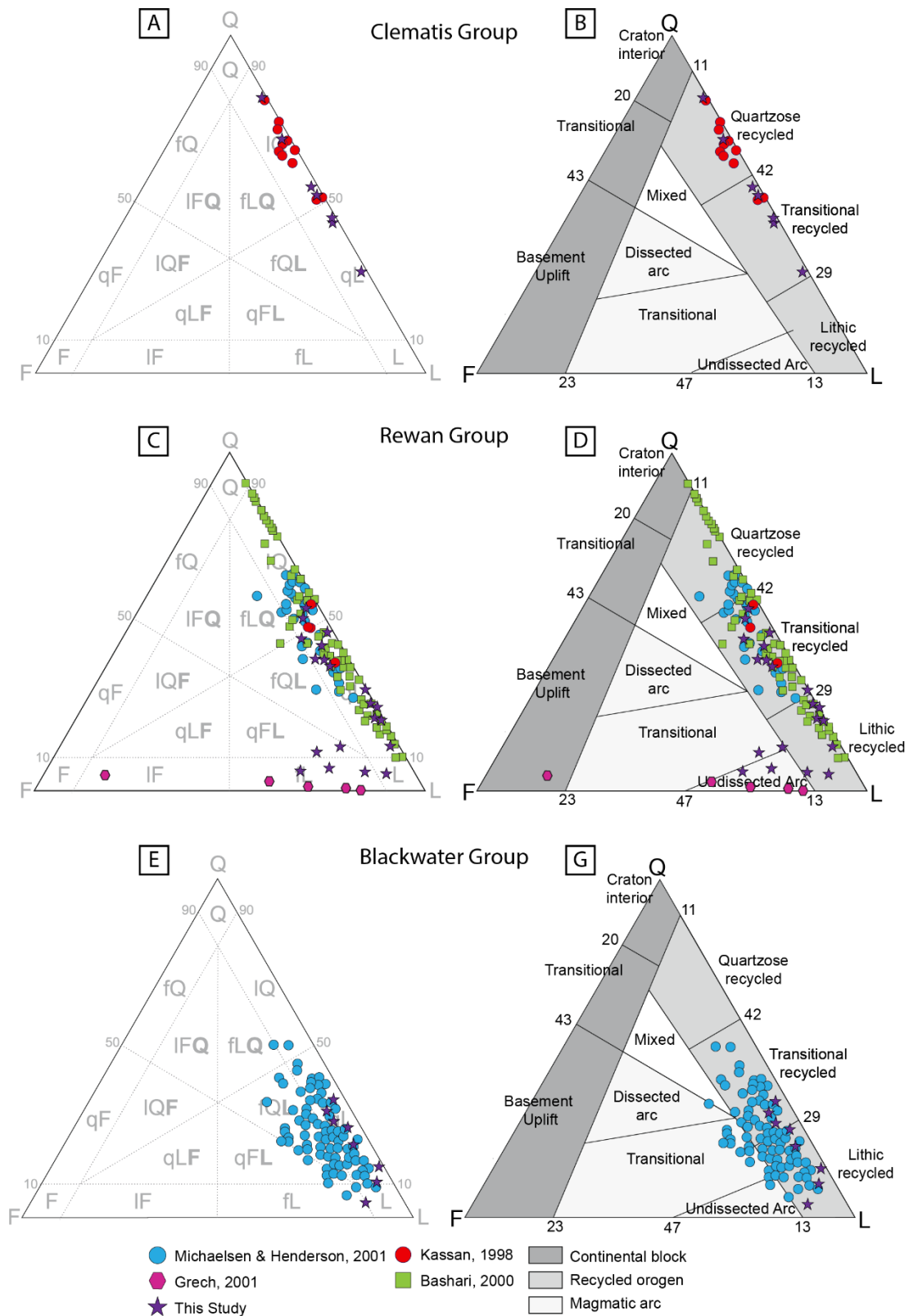
404 Petrographic results are summarised using QFL ternary plots and Dickinson-style provenance  
405 fields (Figure 3) with representative thin-section images (Figures 4 and 5). Across units, most  
406 point-count data plot near the quartz–lithic join, indicating low feldspar contents (Figure 3).

407 Blackwater Group samples plot towards the lithic-rich side of QFL space and cluster  
408 near the quartz–lithic join (Figure 3A). In the provenance discrimination plot, they fall mainly  
409 within transitional to lithic recycled fields (Figure 3B). The Bandanna Formation thin section  
410 shows abundant lithic grains and calcite cement (Figure 4A).

411 Rewan Group samples show broader dispersion along the quartz–lithic axis and plot  
412 closer to the lithic corner than Clematis Group samples (Figure 3C). In the Dickinson diagram,  
413 Rewan Group samples plot mainly in transitional recycled and magmatic-arc fields (Figure  
414 3D). Thin sections from the Sagittarius Sandstone contain volcanic rock fragments and  
415 feldspar, and carbonate cement is locally present (Figure 4B–D). Arcadia Formation thin  
416 sections show the same framework components, with zircon as an accessory phase and local  
417 carbonate cement (Figure 5A–B). The new Rewan Group point counts overlap the compiled  
418 datasets plotted in Figure 3 and extend coverage for samples from the Taroom Trough.

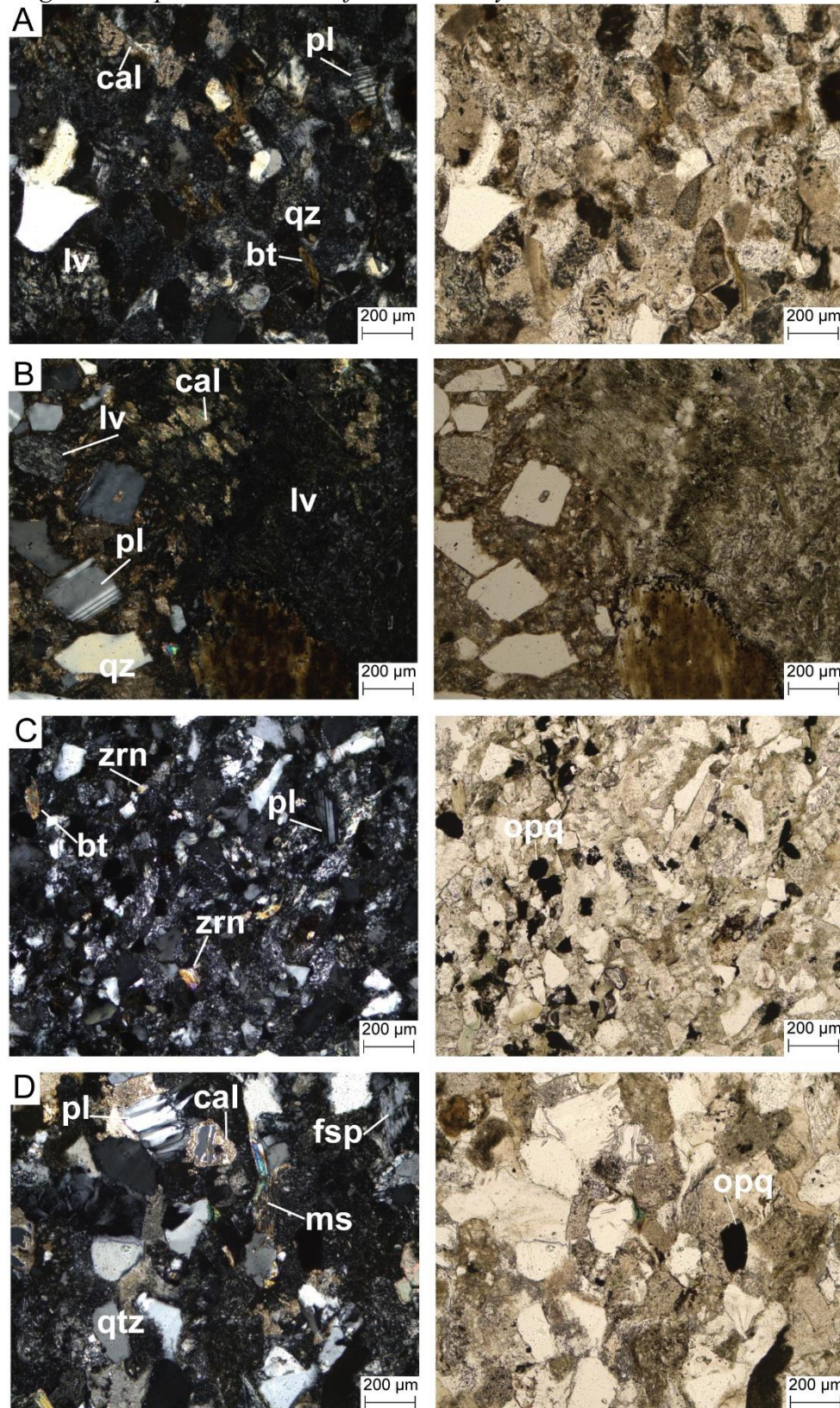
419 Clematis Group samples plot towards the quartz-rich side of the QFL diagram and fall  
420 mainly within quartzose recycled to transitional recycled fields (Figure 3E–F). Thin sections

421 from the Clematis Group show quartz-rich frameworks with subordinate feldspar and variable  
 422 lithic fragments (Figure 5C–D).



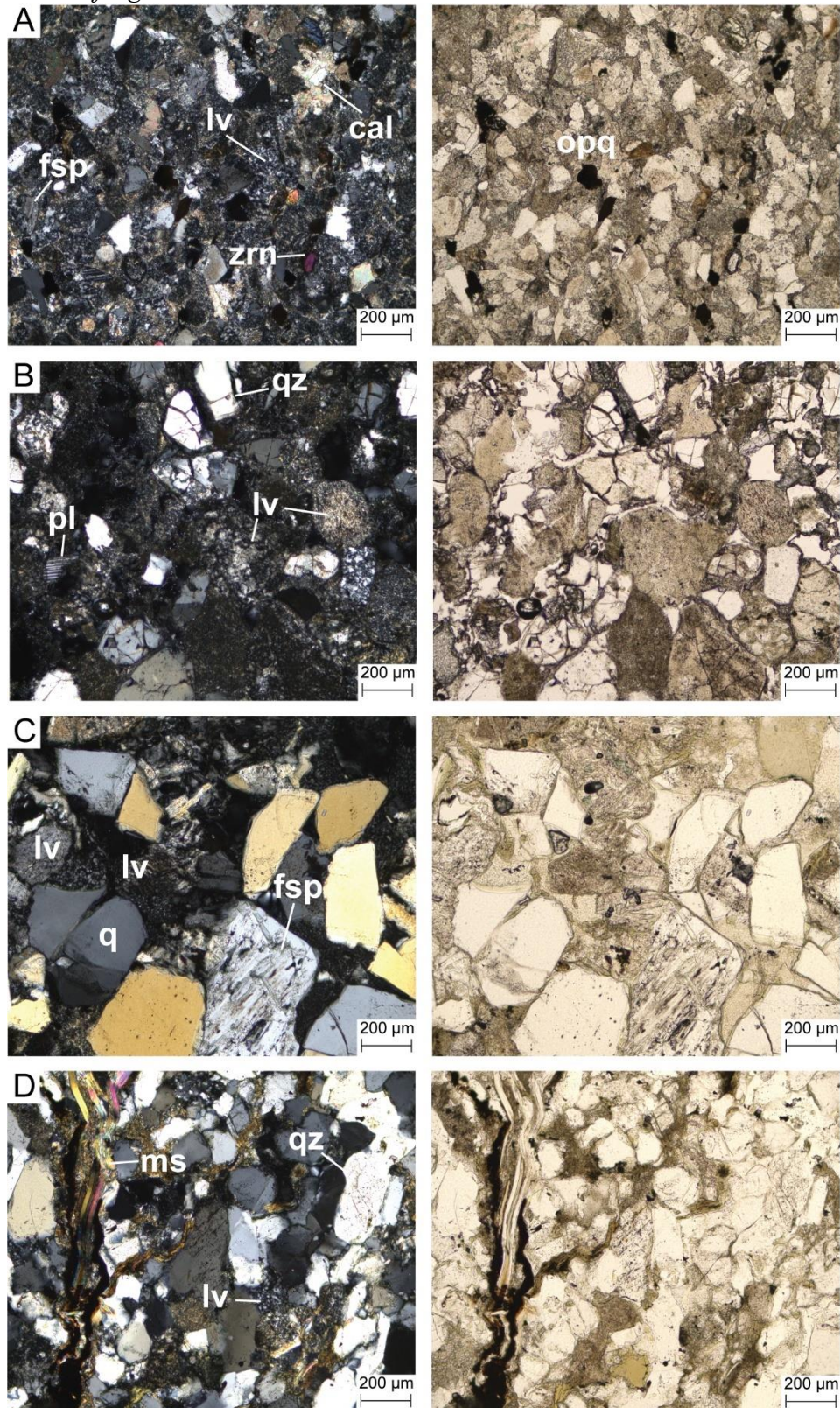
423 **Figure 3.** Quartz–feldspar–lithic classification diagrams (A, C, E) use the sandstone  
 424 classification of Garzanti (2016, 2019). Provenance discrimination diagrams (B, D, F) follow  
 425 Dickinson and Suczek (1979) and Dickinson et al. (1983) and show continental block, recycled

426 orogen, and magmatic arc fields. Panels A–B show Blackwater Group samples, panels C–D  
427 show Rewan Group samples, and panels E–F show Clematis Group samples. Data compiled  
428 from Kassan (1994), Bashari (2000), Michaelsen & Henderson (2000), and Grech (2001) are  
429 plotted alongside new point-count data from this study.



430 **Figure 4.** Paired images show cross-polarised light (left; XPL) and plane-polarised light  
431 (right; PPL) views for each sample. (A) Taroom 8, 552 m (Bandanna Formation). (B) Theodore

432 NS150, 171 m (Sagittarius Sandstone). (C) Drake NS 27, 131 m (Sagittarius Sandstone). (D)  
433 Taroom 8, 408 m (Sagittarius Sandstone). Mineral abbreviations: **bt** = biotite; **cal** = calcite;  
434 **opq** = Fe-oxide/opaque grain; **fsp** = feldspar; **ms** = muscovite; **pl** = plagioclase; **qz** = quartz;  
435 **lv** = volcanic rock fragment; **zrn** = zircon.



436 **Figure 5.** Paired images show cross-polarised light (left; XPL) and plane-polarised light  
437 (right; PPL) views for each sample. (A) Taroom 14, 1144 m (Arcadia Formation). (B) Taroom

438 8, 217 m (*Arcadia Formation*). (C) Taroom 13, 765 m (*Clematis Group*). (D) Taroom 14, 904  
439 m (*Clematis Group*). Mineral abbreviations: **bt** = biotite; **cal** = calcite; **opq** = Fe-oxide/opaque  
440 grain; **fsp** = feldspar; **ms** = muscovite; **pl** = plagioclase; **qz** = quartz; **lv** = volcanic rock  
441 fragment; **zrn** = zircon.

442 **Table 1.** Petrographic characteristics of sandstone samples summarised for each stratigraphic interval. *Q* – quartz, *F* – feldspar, *L* – lithic  
443 fragments

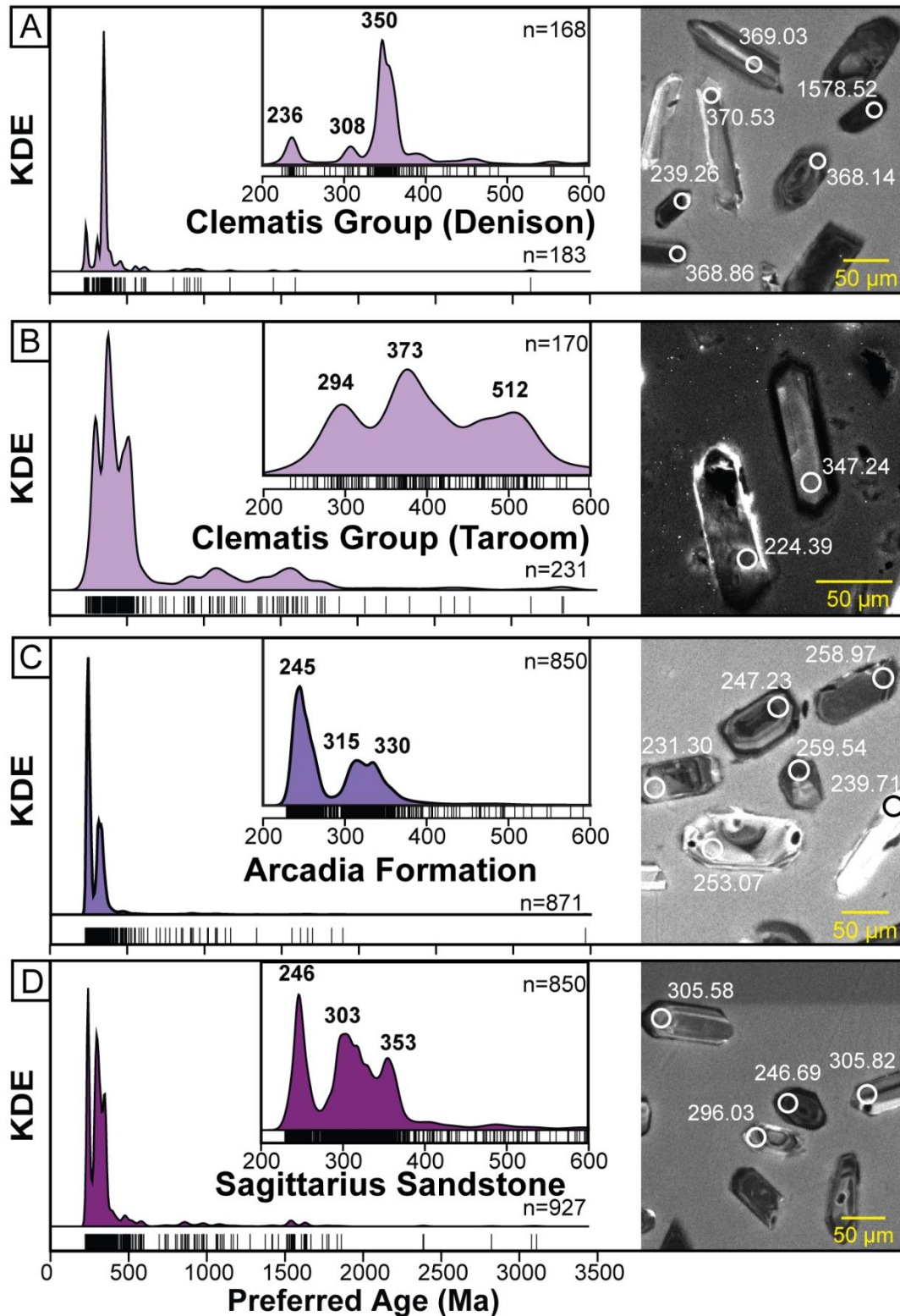
Stratigraphic interval (unit) (n=number of samples)	QFL %	Quartz properties	Grain size	Cements, porosity and matrix	Textural maturity	Lithic grains	Accessory minerals	Ref. figure(s)
Blackwater Group (n=7)	Q: 10.4–34.6% F: 1.2–6.3% L: 62.3–85.7%	Both mono- and polycrystalline varieties present	Fine to medium grained sand	Calcite cement occurs in this study's Bandanna panel.	Low to moderate	Volcanic lithic fragments dominate	Biotite present; minor opaques and zircons.	Fig. 4A
Sagittarius Sandstone (tuffaceous debris flow; GSQ Theodore NS150) (n=2)	Q 5.7–6.4% F 21.3–29.1% L 65.2–72.3%	minor mono- and polycrystalline varieties	Fine grained to pebbles	Carbonate occurs as cement and as an alteration product; chlorite alteration is strong	Immature (angular, poorly sorted; limited reworking)	Dominated by igneous rock fragments, including abundant trachyte; basaltic fragments noted; plagioclase is euhedral and twinned (volcanic origin)	Zircon and mica occur as accessory phase; minor pyrite	Fig. 4B
Sagittarius Sandstone (fluvial sandstones) (n=12)	Q 4.7–50.9% F 0.6–22.2% L 43.4–87.8%	Monocrystalline quartz dominates and minor polycrystalline varieties present	Fine to medium grained sand	Calcite pore-filling cement and early siderite occur in Rewan lithic sandstones regionally	Low to moderate	Volcanic lithics dominate many intervals	Authigenic phases in Rewan lithic sandstones include calcite, siderite, chlorite, kaolin/illite (context for cement/matrix expectations)	Fig. 4 C-D
Arcadia Formation (n=6)	Q: 20.6–53.9% F: 0.0–8.6% L: 42.5–78.5%	Monocrystalline quartz dominates and minor polycrystalline varieties present	Fine to medium grained sand	Calcite is a common pore-filling cement; siderite and quartz overgrowths may occur	Low to moderate; typically, subangular grains	Volcanic lithic fragments dominate and sporadic chert	Muscovite, zircon present, feldspar (incl. plagioclase)	Fig. 5 A-B
Clematis Group (n=7)	Q: 30.1–81.4% F: 1.2–2.6% L: 17.0–68.4%	Monocrystalline quartz dominates	Fine to very coarse-grained sand	Patchy cement and variable matrix; porosity varies between samples.	Low to moderate	Mostly sparse lithics in quartzose intervals; where present, volcanic fragments occur (this study).	Muscovite common in Clematis; zircon present as an accessory phase.	Fig. 5 C-D

## 444 **4.2 Detrital zircon age spectra**

445 Detrital zircon U–Pb results are presented for 12 sandstone samples from the Rewan  
446 Group and Clematis Group. Sample locations are shown in Figure 1 and the stratigraphic  
447 grouping is summarised in Figure 2. Age spectra are shown as formation-level composites  
448 (Figure 6) and for the full dataset (Figure 7A). Samples from the same stratigraphic unit were  
449 combined to summarise unit-scale detrital signatures, and concordant analyses were also  
450 grouped into broad age-population bins for percentage comparison (Table 2).

451 The filtered Bowen Basin dataset includes 2212 grains. These are partitioned into 927  
452 grains from the Sagittarius Sandstone, 871 grains from the Arcadia Formation, 183 grains from  
453 the Clematis Group in the Denison Trough, and 231 grains from the Clematis Group in the  
454 Taroom Trough (Figure 6). The combined spectrum is dominated by Phanerozoic ages, with  
455 the highest densities between ca. 200 and 450 Ma and subordinate older Palaeozoic and  
456 Proterozoic components (Figure 7A). Modes in the full dataset occur near ca. 245 Ma, ca. 312  
457 Ma, and ca. 341 Ma (Figure 7A).

458 The Sagittarius Sandstone is characterised by a dominant Triassic mode near *ca.* 246  
459 Ma and secondary modes near *ca.* 303 Ma and *ca.* 353 Ma (Figure 6D). The overlying Arcadia  
460 Formation shows a dominant Triassic mode near *ca.* 245 Ma with secondary modes near *ca.*  
461 315 Ma and *ca.* 330 Ma (Figure 6C). In both Rewan Group units, the *ca.* 200–400 Ma interval  
462 dominates the spectra, but the relative balance within that interval differs between the two  
463 formations. In the grouped percentage summary, 28.5% of grains from the Sagittarius  
464 Sandstone fall within the 220–285 Ma bin and 55.9% within the 285–400 Ma bin, whereas  
465 grains from the Arcadia Formation fall at 52.2% and 40.6%, respectively (Table 2). The Arcadia  
466 Formation contains a larger younger Triassic component, whereas the Sagittarius Sandstone  
467 retains a larger older Palaeozoic component.



468 **Figure 6.** Kernel density estimates (KDEs) show preferred U–Pb age distributions for (A)  
 469 Clematis Group (Denison Trough), (B) Clematis Group (Taroom Trough), (C) Arcadia  
 470 Formation (basin-wide), and (D) Sagittarius Sandstone (Sst.; basin-wide). Insets highlight the  
 471 <600 Ma portion of each spectrum. Tick marks show individual analyses; n shows the number  
 472 of grains plotted and inset n values refer to grains younger than 600 Ma. Cathodoluminescence  
 473 images adjacent to each KDE show representative zircon grains from the corresponding  
 474 sample group, illustrating typical internal zoning, and spot locations used for U–Pb analyses  
 475 and their corresponding ages (in Ma).

476 The Clematis Group in the Denison Trough is dominated by a mode near ca. 350 Ma  
477 with a smaller component near ca. 308 Ma and a minor Triassic component near ca. 236 Ma  
478 (Figure 6A). The Clematis Group in the Taroom Trough is characterised by modes near ca. 294  
479 Ma, ca. 373 Ma, and ca. 512 Ma, and it lacks a dominant Triassic mode comparable to the  
480 Rewan Group (Figure 6B). This difference is also expressed in the grouped percentages. Only  
481 6.5% of the grains from the Clematis Group in the Taroom Trough fall within the 220–285 Ma  
482 bin, and 55.8% are older than 400 Ma. The Clematis Group in the Denison Trough is less  
483 extreme: 12.0% of grains fall within the 220–285 Ma bin and 72.1% within the 285–400 Ma  
484 bin (Table 2).

485 Lag-time plots (crystallisation age minus depositional age) also differ between the  
486 Rewan Group and the Clematis Group (Figure 7B). Rewan Group curves rise steeply at low  
487 lag values, whereas Clematis Group curves rise more gradually and extend further into longer  
488 lag times. Because the depositional constraints are MDAs, these lag values represent lower  
489 bounds on the true lag time.

490 Between-sample similarity was evaluated using multidimensional scaling (MDS)  
491 derived from a Wasserstein-2 dissimilarity matrix (Figure 9A). Most Sagittarius Sandstone and  
492 Arcadia Formation samples plot close together and overlap in MDS space (Figure 9A).  
493 Clematis Group samples plot away from this main Rewan Group cluster (Figure 9A).

494 MDA are summarised using multiple estimators (Table 3). Rewan Group MLA  
495 estimates fall within the Triassic and differ among sample groups. Arcadia Formation samples  
496 yield MLA estimates that fall in a narrow range of ca. 239–236 Ma (Table 3). Sagittarius  
497 Sandstone samples show a wider spread in MLA estimates, with samples from the Denison  
498 Trough yielding MLA estimates of ca. 238–233 Ma and samples from the Taroom Trough and  
499 Brumby Plains 1 yielding older MLA estimates, including BP1-24-02 at  $244.43 \pm 1.55$  Ma and  
500 BP1-24-03 at  $250.2 \pm 2.3$  Ma (Table 3). For the Clematis Group, the Denison Trough sample

501 (CT-24-01) yields an MLA estimate of  $227.1 \pm 6.1$  Ma and retains a minor Triassic component,  
502 whereas the Taroom Trough sample (T14-25-07) contains few Triassic grains and is dominated  
503 by older Palaeozoic ages (Figure 6A, B; Table 3). Across samples, YSG estimates are typically  
504 younger than multi-grain estimators and MLA, so all estimators are reported together to  
505 document estimator spread and to enable direct comparison among samples (Table 3).

506  
507 **Table 2.** Percentage and grain-count summary of broad detrital zircon age populations for the  
508 Sagittarius Sandstone, Arcadia Formation, and Clematis Group composites shown in Figure  
509 6. Values are based on concordant grains only, with counts in parentheses. The table provides  
510 a simplified comparison of relative age-population abundance among the four composite  
511 spectra.

Age population	Sagittarius Sandstone (n=927)	Arcadia Formation (n=871)	Clematis Group, Taroom Trough (n=231)	Clematis Group, Denison Trough (n=183)
Hunter Bowen Orogeny (220-<285 Ma)	28.5 % (264)	52.2 % (455)	6.5 % (15)	12.0 % (22)
New England Orogen (285-<400 Ma)	55.9 % (518)	40.6 % (354)	32.9 % (76)	72.1 % (132)
Older Tasmanides (400-<500 Ma)	4.6 % (43)	2.5 % (22)	21.6 % (50)	6.6 % (12)
Pacific-Gondwana (500-<650 Ma)	2.7 % (25)	1.1 % (10)	13.0 % (30)	3.8 % (7)
Grenville Orogen (850-<1250 Ma)	3.1 % (29)	1.7 % (15)	9.5 % (22)	3.8 % (7)
North Australian Craton (1450-<1950 Ma)	3.2 % (30)	0.7 % (6)	8.7 % (20)	0.5 % (1)
Older cratonic grains (1950-3500 Ma)	0.9 % (8)	0.1 % (1)	3.0 % (7)	0.0 % (0)
Unassigned / other	1.1 % (10)	0.9 % (8)	4.8 % (11)	1.1 % (2)

512

## 513 5. Discussion

514

### 515 5.1 Provenance of the Northern Bowen Basin

516

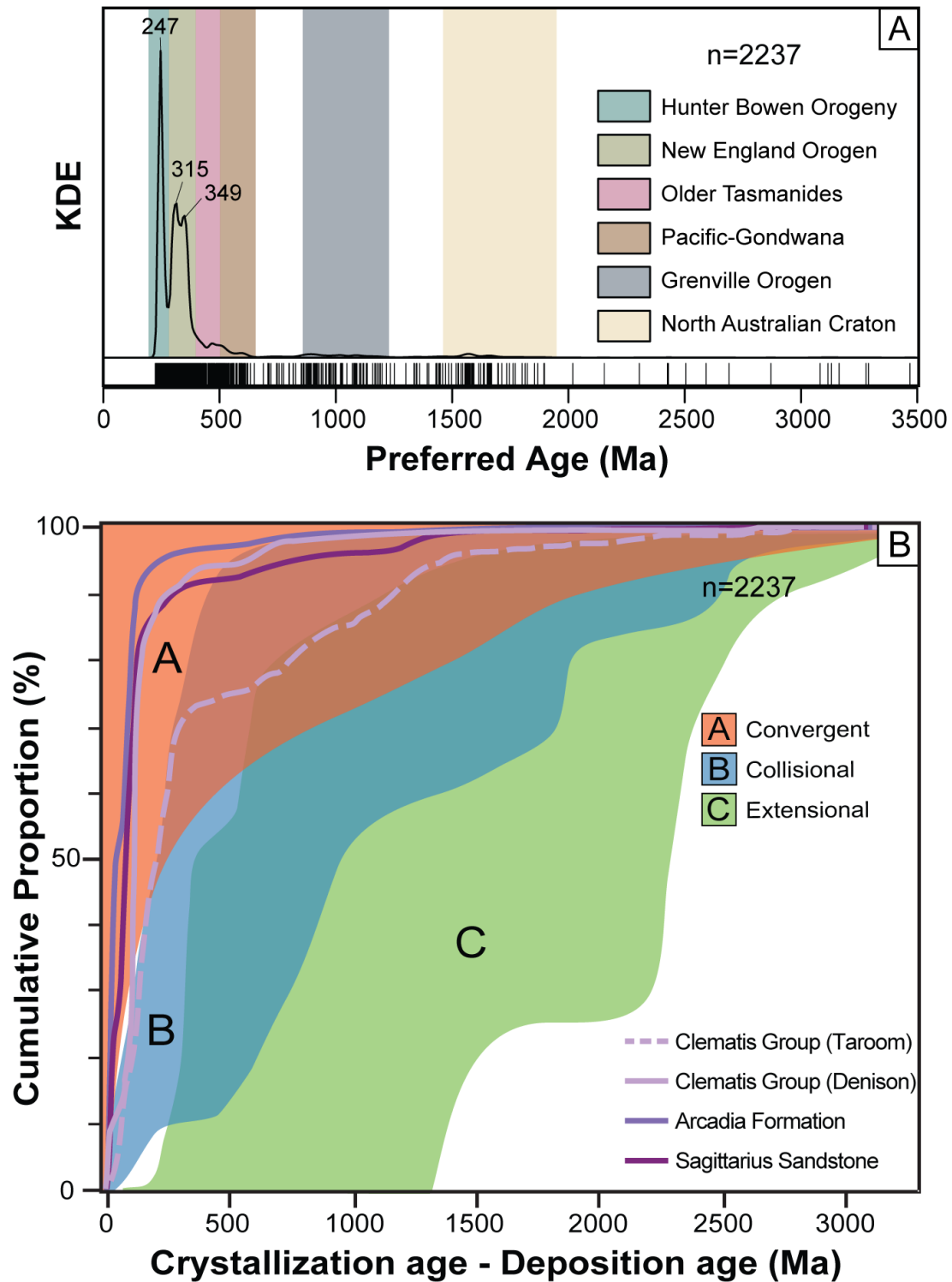
#### 517 5.1.1 Sandstone Petrography

518 Across the succession, most samples plot along the quartz–lithic side of the diagram  
519 and feldspar is generally minor (Figure 3). Feldspar-poor compositions are therefore treated as  
520 supportive, but not diagnostic, of limited input from fresh feldspar-rich plutonic sources. The  
521 main petrographic change is an up-section shift from lithic-rich Blackwater Group and Rewan  
522 Group sandstones to more quartz-rich, but still feldspar-poor, Clematis Group sandstones.

523 Late Permian Blackwater Group samples show that feldspar-poor, lithic-rich  
524 compositions were already established before deposition of the Triassic succession (Figure 3A-  
525 B, 4A; Michaelsen & Henderson, 2000). Their overlap with Rewan Group QFL fields may  
526 reflect continued erosion from similar source rocks, recycling of older basin fill, or both.  
527 Petrography alone does not distinguish between those alternatives.

528 Rewan Group sandstones are likewise feldspar poor but extend to lower-quartz and  
529 higher-lithic compositions, consistent with volcanoclastic-rich Rewan Group petrofacies  
530 (Figure 3C, D; Table 1; Bashari, 2000; Michaelsen & Henderson, 2000). A subset of Sagittarius  
531 Sandstone samples from Theodore NS150 is compositionally distinct and plots at very low  
532 quartz with elevated feldspar and volcanic lithic contents relative to the rest of the Rewan  
533 Group (Figure 4B). Grech (2001) interpreted comparable feldspar-rich, tuffaceous beds there  
534 as syndepositional volcanic input. Its position on the eastern margin of the Taroom Trough is  
535 consistent with that interpretation, although local ash-fall reworking and facies-controlled  
536 concentration remain viable alternatives.

537 Clematis Group samples record the clearest up-section petrographic shift. They are  
538 more quartz rich, remain feldspar poor, and plot mainly in quartzose to transitional recycled  
539 fields, consistent with previous descriptions of the unit (Figure 3E-F; Kassan, 1994). The  
540 change is therefore not from lithic-rich to feldspathic sandstones, but from lithic-rich, feldspar-  
541 poor sandstones to more quartz-rich, still feldspar-poor sandstones. Comparable up-section  
542 shifts towards more quartz-rich and recycled compositions have been described in other  
543 retroarc foreland basins and are commonly linked to changes in source access, recycling, and  
544 drainage organisation (DeCelles & Burden, 1992; Dutta & Wheat, 1993; Gómez et al., 2019;  
545 Maravelis et al., 2023).



546 **Figure 7.** (A) Kernel density estimate (KDE) of preferred U–Pb ages for all concordant detrital  
 547 zircon analyses from this study ( $n = 2212$ ), with shaded bands indicating broad age domains  
 548 commonly associated with regional source terranes and tectonic provinces (Hunter–  
 549 Bowen/New England Orogen, older Tasmanides, Pacific–Gondwana, Grenville, and North  
 550 Australian craton). (B) Cumulative proportion plot of crystallisation age minus depositional  
 551 age (lag time) for individual samples, modified after the conceptual framework of Cawood *et*  
 552 *al.* (2012) to illustrate relative contributions from convergent-margin, collisional, and  
 553 extensional source settings.

### 554 **5.1.2 Detrital Zircon Geochronology**

555 Detrital zircon age spectra from Triassic sandstones in the northern Bowen Basin are  
556 dominated by Permian–Triassic and Carboniferous populations (Figures 6 and 7A). When  
557 Rewan Group samples are pooled, the dataset is characterised by three principal modes at ca.  
558 245 Ma, 312 Ma, and 341 Ma (Figure 7A), consistent with sustained sediment supply from the  
559 active Tasmanide margin with subordinate contributions from older terranes from the east. The  
560 Sagittarius Sandstone and Arcadia Formation share the same main age populations, but they  
561 are not identical. The Sagittarius Sandstone retains stronger older Palaeozoic modes, whereas  
562 the Arcadia Formation is more strongly dominated by its ca. 245 Ma Triassic peak (Figure 6C,  
563 D; Table 2). The Arcadia Formation’s provenance is therefore more strongly dominated by the  
564 younger Triassic population, whereas the Sagittarius Sandstone retains a larger older  
565 Palaeozoic component. In MDS space, most Sagittarius Sandstone and Arcadia Formation  
566 samples occupy the same Rewan Group field, but the Sagittarius Sandstone spans a broader  
567 range of positions (Figure 9A), indicating greater internal variability. The percentage data show  
568 a stronger relative contribution from the younger population in the Arcadia Formation, but they  
569 do not by themselves measure absolute volcanic flux.

570 The dominant Middle Triassic zircon component in the Rewan Group is most simply  
571 explained by derivation from margin-proximal igneous sources associated with the Permian–  
572 Triassic magmatic belt of the New England Orogen and related arc-to-retroarc systems (Figure  
573 7A). This interpretation is consistent with the feldspar-poor, lithic-rich petrography of the  
574 Rewan Group. Together, the DZ spectra and QFL data indicate substantial input from eastern,  
575 margin-proximal sources, including contemporaneous volcanic and volcanic–plutonic material  
576 during Rewan Group deposition.

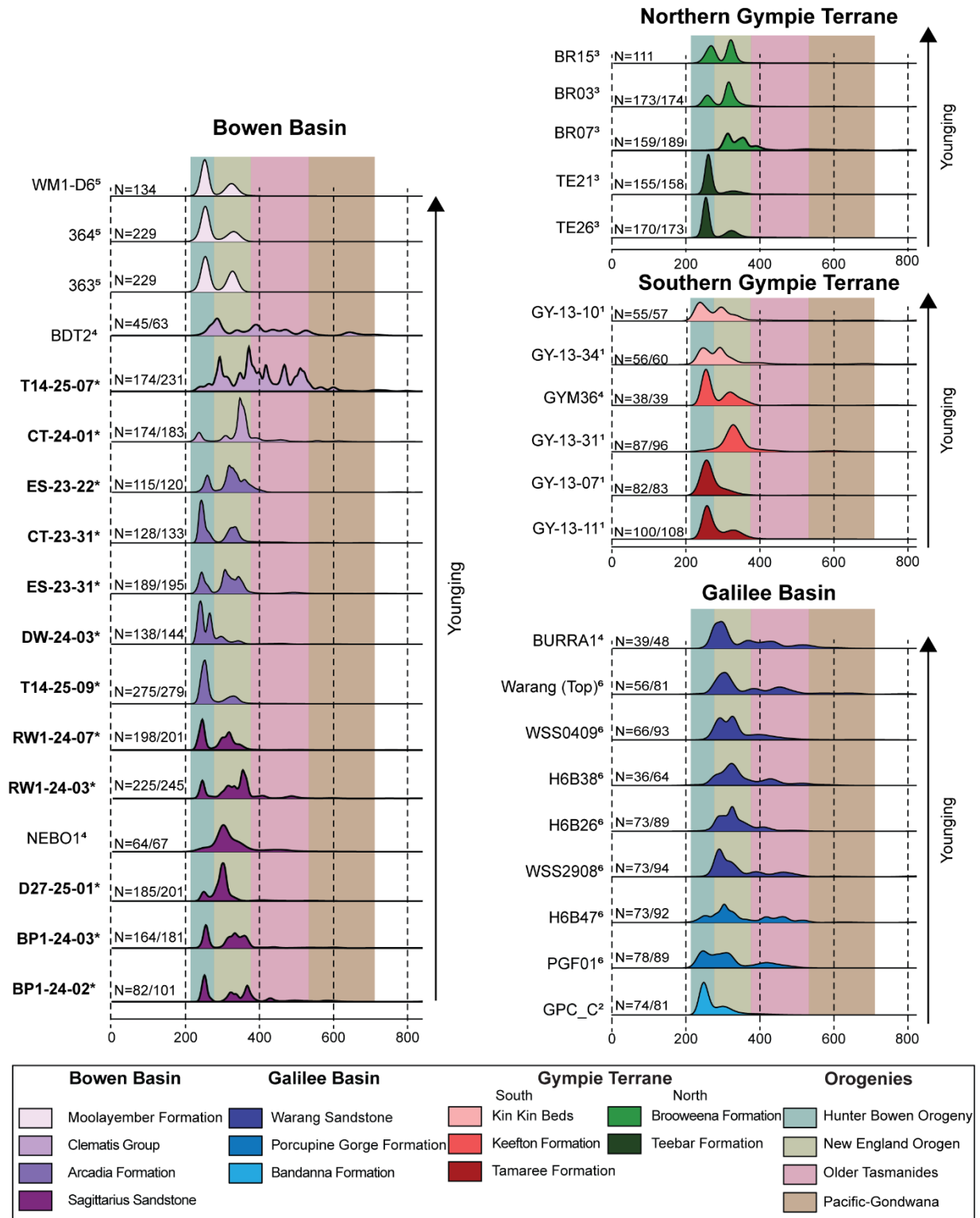
577 Carboniferous–Permian and older Palaeozoic zircon components require contributions  
578 from older Tasmanide source rocks and/or multicycle sediment pathways. These age ranges

No.	Sample	Formation	Location	Literature	YSG ( $\pm 2\sigma$ ) (Ma)	YGC ( $\pm 2\sigma$ ) (Ma)	MLA ( $\pm 2\sigma$ ) (Ma)
1	WM1-D6	Moolayember Formation	Bowen Basin	Sobczak et al., 2022	219.4 $\pm$ 7.1	245.7 $\pm$ 1.7; MSWD 0.77; 26 grains	236.7 $\pm$ 3.7
2	364	Moolayember Formation	Bowen Basin	Sobczak et al., 2022	183.5 $\pm$ 4.4	233.9 $\pm$ 0.9; MSWD 1.55; 6 grains	200.8 $\pm$ 4.8
3	363	Moolayember Formation	Bowen Basin	Sobczak et al., 2022	217.7 $\pm$ 1.5	234.1 $\pm$ 1.6; MSWD 0.80; 3 grains	220.0 $\pm$ 1.8
4	BDT2	Clematis Group	Bowen Basin	Adams et al., 2022	248.0 $\pm$ 4.3	265.2 $\pm$ 1.0; MSWD 1.1; 5 grains	261.5 $\pm$ 21.0
5	T14-25-07*	Clematis Group	Bowen Basin	This study	233.06 $\pm$ 4.3	237.8 $\pm$ 4.1; MSWD 0.2; 3 grains	238.5 $\pm$ 8.1
6	CT-24-01*	Clematis Group	Bowen Basin	This study	223.83 $\pm$ 6.9	229.3 $\pm$ 3.8; MSWD 1.7; 7 grains	227.1 $\pm$ 6.1
7	ES-23-22*	Arcadia Formation	Bowen Basin	This study	233.89 $\pm$ 4.7	247.3 $\pm$ 2.5; MSWD 1.01; 6 grains	236.7 $\pm$ 3.7
8	CT-23-31*	Arcadia Formation	Bowen Basin	This study	231.48 $\pm$ 5.6	237.0 $\pm$ 1.0; MSWD 1.6; 15 grains	239.5 $\pm$ 2.7
9	ES-23-31*	Arcadia Formation	Bowen Basin	This study	229.26 $\pm$ 10.3	236.2 $\pm$ 2.1; MSWD 0.82; 13 grains	239.2 $\pm$ 3.2
10	DW-24-03*	Arcadia Formation	Bowen Basin	This study	228.50 $\pm$ 6.2	233.2 $\pm$ 1.3; MSWD 0.77; 24 grains	235.8 $\pm$ 2.1
11	T14-25-09*	Arcadia Formation	Bowen Basin	This study	230.52 $\pm$ 4.3	234.9 $\pm$ 1.2; MSWD 0.64; 18 grains	237.7 $\pm$ 1.7
12	RW1-24-03*	Sagittarius Sandstone	Bowen Basin	This study	230.79 $\pm$ 7.3	236.7 $\pm$ 1.3; MSWD 1.1 ; 14 grains	237.7 $\pm$ 2.5
13	RW1-24-07*	Sagittarius Sandstone	Bowen Basin	This study	230.17 $\pm$ 4.8	234.3 $\pm$ 1.1; MSWD 1.2; 27 grains	233.3 $\pm$ 2.1
14	NEBO1	Sagittarius Sandstone	Bowen Basin	Adams et al., 2022	244.0 $\pm$ 3.0	249.7 $\pm$ 2.5; MSWD 1.3; 6 grains	248.0 $\pm$ 6.6
15	D27-25-01*	Sagittarius Sandstone	Bowen Basin	This study	242.48 $\pm$ 5.8	246.7 $\pm$ 1.4; MSWD 0.61; 18 grains	246.0 $\pm$ 1.9
16	BP1-24-03*	Sagittarius Sandstone	Bowen Basin	This study	241.11 $\pm$ 6.0	247.8 $\pm$ 1.5; MSWD 0.98; 22 grains	250.2 $\pm$ 2.3
17	BP1-24-02*	Sagittarius Sandstone	Bowen Basin	This study	236.09 $\pm$ 5.9	242.1 $\pm$ 1.5; MSWD 1.07; 17 grains	244.43 $\pm$ 1.6
18	BURRA1	Warang Sandstone	Northeastern Galilee Basin	Adams et al., 2022	259.0 $\pm$ 4.0	275.8 $\pm$ 2.4; MSWD 0.98; 8 grains	274.2 $\pm$ 3.2
19	Warang Top	Warang Sandstone	Northeastern Galilee Basin	Todd et al., 2022	244.6 $\pm$ 4.9	276.4 $\pm$ 2.6; MSWD 1.15; 6 grains	246.6 $\pm$ 11.4
20	WSS0409	Warang Sandstone	Northeastern Galilee Basin	Todd et al., 2022	265.5 $\pm$ 5.0	273.9 $\pm$ 4.7; MSWD 1.15; 6 grains	280.6 $\pm$ 8.9
21	H6B38	Warang Sandstone	Northeastern Galilee Basin	Todd et al., 2022	232.0 $\pm$ 2.5	280.4 $\pm$ 3.8; MSWD 1.04; 5 grains	232.0 $\pm$ 7.4
22	H6B26	Warang Sandstone	Northeastern Galilee Basin	Todd et al., 2022	247.6 $\pm$ 3.1	272.4 $\pm$ 3.8; MSWD 2.03; 3 grains	248.0 $\pm$ 7.5
23	WSS2908	Warang Sandstone	Northeastern Galilee Basin	Todd et al., 2022	242.7 $\pm$ 3.9	274.1 $\pm$ 3.8; MSWD 1.04; 5 grains	244.5 $\pm$ 9.1
24	H6B47	Porcupine Gorge Formation	Northeastern Galilee Basin	Todd et al., 2022	223.4 $\pm$ 10.7	238.7 $\pm$ 3.0; MSWD 0.30; 3 grains	236.9 $\pm$ 5.2
25	PGF01	Porcupine Gorge Formation	Northeastern Galilee Basin	Todd et al., 2022	228.0 $\pm$ 3.0	229.5 $\pm$ 1.8; MSWD 1.79; 3 grains	228.2 $\pm$ 3.3
26	GPC_C	Bandanna Formation	Southern Galilee Basin	Philips et al., 2017	233.0 $\pm$ 13	247.4 $\pm$ 1.9; MSWD 0.75; 43 grains	249.6 $\pm$ 4.1
27	BR15	Brooweena Formation	Northern Gympie Terrane	Rosenbaum et al., 2020	242.3 $\pm$ 11.0	252.6 $\pm$ 1.9; MSWD 1.9; 24 grains	249.3 $\pm$ 6.1
28	BR03	Brooweena Formation	Northern Gympie Terrane	Rosenbaum et al., 2020	237.3 $\pm$ 8.1	245.3 $\pm$ 2.3; MSWD 0.9; 10 grains	247.5 $\pm$ 3.8
29	BR07	Brooweena Formation	Northern Gympie Terrane	Rosenbaum et al., 2020	275.5 $\pm$ 12.0	285.4 $\pm$ 4.8; MSWD 2.1; 5 grains	305.6 $\pm$ 3.3
30	TE21	Teebar Formation	Northern Gympie Terrane	Rosenbaum et al., 2020	243.0 $\pm$ 11.0	253.7 $\pm$ 1.1; MSWD 0.5; 65 grains	257.6 $\pm$ 1.0
31	TE26	Teebar Formation	Northern Gympie Terrane	Rosenbaum et al., 2020	233.0 $\pm$ 11.0	245.6 $\pm$ 2.9; MSWD 0.5; 16 grains	254.9 $\pm$ 1.2
32	GY-13-10	Kin Kin Beds	Southern Gympie Terrane	Li et al., 2015	224.0 $\pm$ 10.6	229.9 $\pm$ 2.9; MSWD 1.1; 10 grains	231.1 $\pm$ 5.0
33	GY-13-34	Kin Kin Beds	Southern Gympie Terrane	Li et al., 2015	225.4 $\pm$ 9.6	230.7 $\pm$ 4.9; MSWD 0.9; 3 grains	238.5 $\pm$ 3.6
34	GYM36	Keefon Formation	Southern Gympie Terrane	Adams et al., 2022	244.0 $\pm$ 6.0	249.7 $\pm$ 1.6; MSWD 1.1; 13 grains	250.6 $\pm$ 1.87
35	GY-13-31	Keefon Formation	Southern Gympie Terrane	Li et al., 2015	249.9 $\pm$ 10.4	256.3 $\pm$ 6.9; MSWD 1.5; 4 grains	252.9 $\pm$ 9.4
36	GY-13-07	Tamaree Formation	Southern Gympie Terrane	Li et al., 2015	235.9 $\pm$ 5.6	241.3 $\pm$ 2.2; MSWD 0.7; 16 grains	244.8 $\pm$ 4.7
37	GY-13-11	Tamaree Formation	Southern Gympie Terrane	Li et al., 2015	242.9 $\pm$ 9.0	250.3 $\pm$ 1.7; MSWD 1.0; 30 grains	250.4 $\pm$ 2.0

579 **Table 3.** Summary of detrital zircon age data and maximum depositional age estimates from this study and from compiled previous studies.

580 are common within the broader Tasmanide orogenic belt and can also be introduced through  
581 recycling of late Palaeozoic basin fill. Recycling is viable in the Bowen Basin because  
582 contractional deformation and structural reactivation affected the Permian–Triassic succession,  
583 generating local uplift and erosion that could remobilise older sedimentary packages (Korsch  
584 et al., 2009). Minor Proterozoic zircon populations occur across the dataset (Figure 7A),  
585 consistent with limited cratonward input and/or recycling from older successions. At the scale  
586 resolved by DZ alone, the older component does not uniquely distinguish between direct  
587 erosion of exposed basement provinces and recycling through Permian sedimentary  
588 successions.

589         The clearest shift from the Rewan Group occurs in the Clematis Group of the Taroom  
590 Trough. Its spectrum lacks the dominant *ca.* 240–250 Ma peak that characterises the Rewan  
591 Group and is instead dominated by older Palaeozoic modes at *ca.* 294, 373, and 512 Ma (Figure  
592 6B). The grouped percentages show the same pattern, with only 6.5% of grains from the  
593 Clematis Group in the Taroom Trough falling in the 220–285 Ma bin, whereas 55.8% are older  
594 than 400 Ma (Table 2). The Clematis Group in the Denison Trough is less extreme. It retains a  
595 minor *ca.* 236 Ma component but is dominated by the 285–400 Ma population, which accounts  
596 for 72.1% of its grains (Figure 6A; Table 2). This shift is consistent with the more quartzose,  
597 feldspar-poor petrography of the Clematis Group. In MDS space, Clematis Group samples span  
598 a wider range and include points displaced from the Rewan Group cluster (Figure 9A).  
599 Clematis Group lag curves show a lower proportion of short crystallisation–deposition age gaps  
600 than the Rewan Group (Figure 7B), using MLA-based MDAs as the depositional reference.  
601 Overall, these data support reduced near-depositional arc input and greater contributions from  
602 older sources, although recycling remains a competing explanation. This contrast motivates the  
603 next step in interpretation, in which palaeodrainage and sediment-routing models are evaluated  
604 against the spatial structure of the DZ dataset and the basin framework.



605 **Figure 8.** Kernel density estimates (KDEs) show preferred U–Pb age distributions (<800 Ma)  
 606 for Triassic samples from the Bowen Basin (this study and published datasets), the Galilee  
 607 Basin, and the northern and southern Gympie Terrane. Samples are ordered by stratigraphic  
 608 younging within each region; \* denotes samples analysed in this study. References: **1** = Li et  
 609 al. (2015); **2** = Phillips et al. (2017); **3** = Rosenbaum et al. (2020); **4** = Adams et al. (2022); **5**  
 610 = Sobczak et al. (2022); **6** = Todd et al. (2022). N shows the number of grains plotted relative  
 611 to the total number of concordant grains. Shaded vertical bands indicate broad age domains  
 612 associated with regional Tasmanide and cratonward source provinces (see legend).

## 613 **5.2 Sediment routing and palaeodrainage implications**

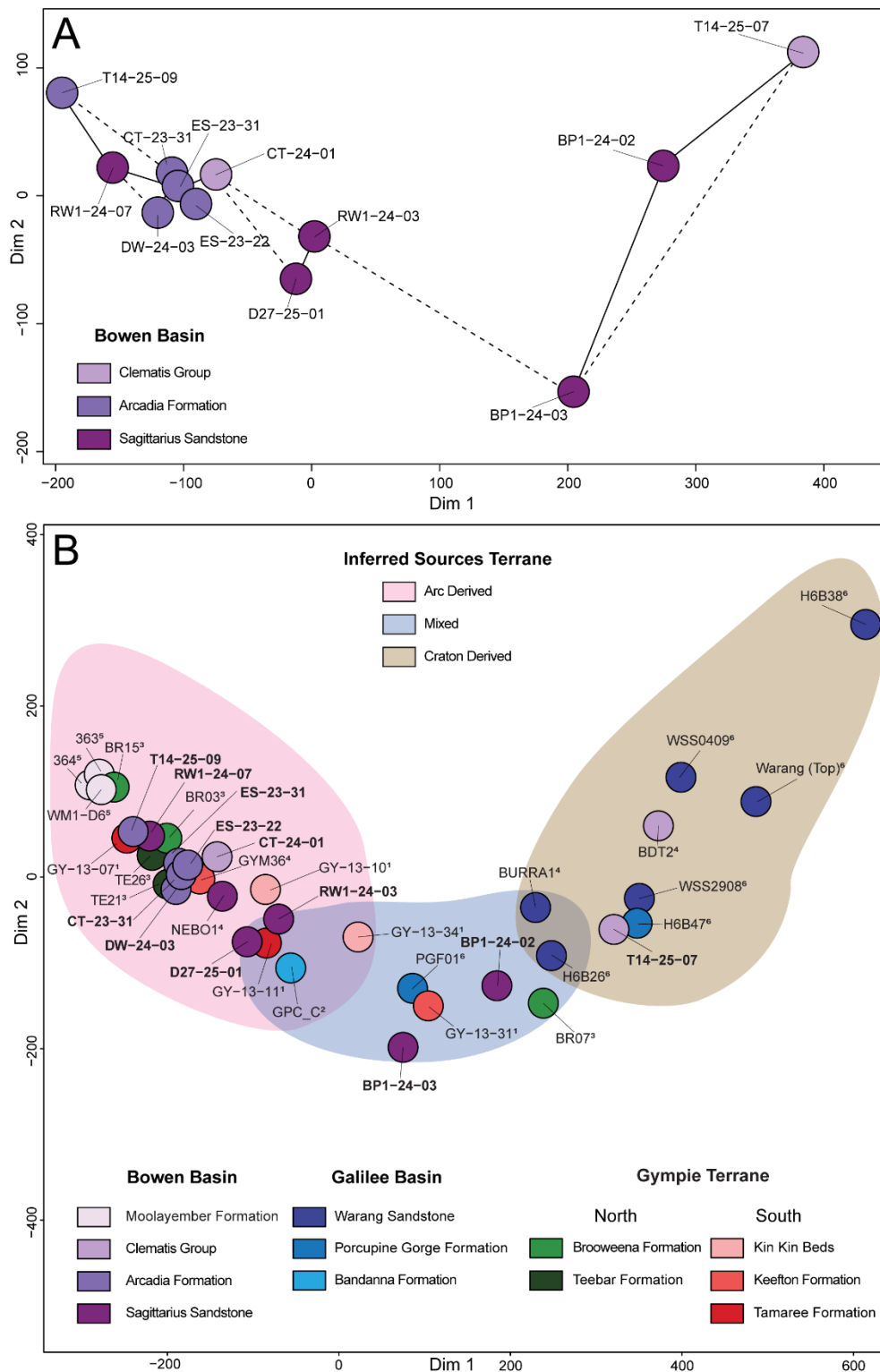
614 Detrital zircon age distributions can be used as basin-scale sediment-routing tracers  
615 because mixtures of age populations preserve information about catchment integration,  
616 recycling, and along-strike mixing that can be compared quantitatively between depocentres  
617 (Mason et al., 2022; Romans et al., 2016; Shaanan et al., 2018; Shaanan & Rosenbaum, 2018).  
618 However, robust routing interpretations require integration of DZ results with independent  
619 sediment-transport constraints, particularly palaeocurrent indicators and basin architecture,  
620 following the approach used in comparable source-to-sink studies (e.g., Tucker et al., 2016).  
621 Here, pairwise spectral dissimilarity is quantified using the Wasserstein-2 distance and  
622 visualised with multidimensional scaling (MDS; Figure 9A). Samples that plot close together  
623 have similar age distributions, whereas those farther apart are more dissimilar. Axis values are  
624 not interpreted directly; instead, similarity is evaluated against the palaeodrainage  
625 reconstruction and within-basin KDE structure (Figures 6, 7, 10).

626 For the Rewan Group, palaeodrainage indicates dominant input from the eastern  
627 margin, with minor western and northwestern contributions routed into trough-confined axial  
628 systems (Figure 10A). This geometry is consistent with an integrated Rewan Group system.  
629 Sagittarius Sandstone and Arcadia Formation samples plot closely in MDS space and show  
630 similar KDE structures dominated by Permian–Triassic and Late Carboniferous populations  
631 (Figures 6C–D, 7A, 9A). Both units are dominated by the 220–400 Ma interval, although the  
632 Arcadia Formation contains a stronger younger component than the Sagittarius Sandstone.  
633 These data indicate that the Rewan Group depositional system remained dominated by eastern  
634 active-margin input, but that the balance between younger and older Palaeozoic populations  
635 varied within the basin. The Carboniferous component may have been derived from northern  
636 provinces such as the Charters Towers Province or Connors Subprovince, and from western  
637 sources such as the Anakie Province (Figure 10; Jell, 2013). These assignments are not unique,

638 and zircon ages alone do not distinguish direct erosion from recycling. The high proportion of  
639 short crystallisation–deposition age gaps in the Rewan dataset (Figure 7B) is consistent with  
640 continued delivery from an active convergent margin source, rather than exclusive recycling  
641 of older basin fill.

642         Although the Rewan Group samples are broadly coherent, the routing system was not  
643 spatially uniform. BP1-24-02 is the clearest Rewan Group offset in Figure 9A, and BP1-24-03  
644 trends in the same direction but less strongly. Relative to the tighter Arcadia Formation cluster  
645 and several Sagittarius Sandstone samples, these spectra retain the Triassic peak but contain  
646 stronger older Palaeozoic components (Figure 8). This part of ordination space is therefore  
647 interpreted as an inferred shift from strongly Triassic-dominated spectra towards mixed spectra  
648 with a larger older Palaeozoic contribution. This interpretation is based on the KDE structure  
649 rather than on the axis alone. In the context of Figure 10A, this behaviour is consistent with  
650 local mixing where east-derived sediment entered trough-confined axial systems and interacted  
651 with sediment delivered from surrounding cratonward terranes. The palaeodrainage model  
652 includes minor sediment inputs from the western and northwestern margins (Figure 10A),  
653 which provide plausible pathways for introducing older zircon components without requiring  
654 a basin-wide change in the dominant source. Structural segmentation into troughs and  
655 intervening highs likely focused axial transport but allowed episodic transverse inputs (Brakel  
656 et al., 2009; Danis et al., 2012; Korsch, Totterdell, Fomin, et al., 2009). This spatial context  
657 also affects recycling potential. Chronostratigraphic constraints indicate more continuous  
658 Triassic accumulation in the Taroom Trough than in the Denison Trough, where non-deposition  
659 and/or erosion is more likely across the Permian–Triassic transition (Scipione et al., 2026).  
660 Where the stratigraphic record is condensed, older units are more likely to be exposed and  
661 available for recycling.

662 Clematis Group samples record a change in routing relative to the Rewan Group, but  
663 the signal varies by depocentre. The palaeodrainage reconstruction suggests reduced east-  
664 derived supply and greater input from western and northwestern continental-interior terranes  
665 during Clematis Group deposition (Figure 10B). The provenance signal supports this inference.  
666 T14-25-07 is separated from the main Rewan Group field in MDS space (Figure 9A) and shows  
667 a distinct KDE structure relative to the Rewan Group, with reduced Permian–Triassic peaks  
668 and greater older Palaeozoic contributions (Figure 6B–D). The Clematis Group in the Taroom  
669 Trough is markedly older-weighted than the Rewan Group, whereas the Clematis Group in the  
670 Denison Trough composite is more intermediate. These differences are consistent with  
671 increased cratonward input and/or recycling, strongest in the Taroom Trough rather than  
672 uniformly across the basin. Potential sources for older Tasmanide-age grains include the  
673 Thomson Basement and recycled Drummond Basin sediments (Figure 10B; Jell, 2013). In lag-  
674 time space, the dataset from the Clematis Group also shifts towards older crystallisation–  
675 deposition offsets (Figure 7B), consistent with increased input from older crustal sources and/or  
676 multicycle recycling. Because recycling can generate similar spectral shifts, routing  
677 interpretations should be tested against structural position, proximity to unconformities, and  
678 additional sampling across depocentres. This shift can be tested against three alternatives,  
679 namely catchment expansion, basin tilting and drainage capture, or increased recycling within  
680 the basin fill. Their relative importance may vary along the troughs.



681 **Figure 9.** Multidimensional scaling (MDS) plots based on pairwise Wasserstein-2 distances  
 682 calculated from detrital zircon age distributions. Distances are visualised in two dimensions,  
 683 where closer points indicate more similar age spectra. Dim 1 and Dim 2 are unitless ordination  
 684 axes and are not interpreted as direct geological variables. (A) MDS for samples analysed in  
 685 this study, coloured by stratigraphic unit. (B) MDS including this study, shown in bold type,  
 686 and published datasets from the Bowen Basin, Galilee Basin, and northern and southern  
 687 Gympie Terrane. Polygons outline inferred arc-dominated, mixed, and craton-dominated fields  
 688 (colour scheme as in Figure 8). **1** = Li et al. (2015); **2** = Phillips et al. (2017); **3** = Rosenbaum  
 689 et al. (2020); **4** = Adams et al. (2022); **5** = Sobczak et al. (2022); **6** = Todd et al. (2022).

### 690 **5.3 Tectonic implications**

691           Rewan Group sandstones include a large fraction of zircons with short crystallisation–  
692 deposition age gaps (Figure 7B), consistent with near-depositional input. The dominance of  
693 Middle Triassic components in Sagittarius Sandstone and Arcadia Formation spectra (Figure  
694 6C–D) and in the basin-wide KDE (Figure 7A) is consistent with continued convergent-margin  
695 magmatism and tectonism along the Tasmanide margin during the Triassic (Jessop et al., 2019;  
696 P. Li et al., 2012; Rosenbaum et al., 2020, 2025). Rosenbaum (2026) interpreted the New  
697 England Orogen as a Middle Permian–Late Triassic continental arc dominated by calc-alkaline  
698 felsic igneous rocks, mainly I-type granitoids, with major magmatic activity beginning at ~270  
699 Ma, peaking at ~252 Ma, and continuing into the Late Triassic. Hf-isotope data from granitoids  
700 of the Permian–Triassic New England Batholith are consistent with this interpretation and  
701 indicate juvenile magmatic input mixed with evolved crustal components in arc-related  
702 magmas (Phillips et al., 2011; Shaw et al., 2011). Regional detrital zircon datasets extend that  
703 pattern beyond the exposed batholith. Tucker et al. (2016) reported a relatively continuous  
704 Triassic–Cretaceous zircon record from eastern Australia with dominantly positive epsilon Hf  
705 ( $\epsilon\text{Hf}$ ) values. Foley et al. (2021) showed that Triassic–Jurassic detrital zircons from eastern  
706 Gondwana are likewise dominated by positive  $\epsilon\text{Hf}$  values that overlap New England Orogen  
707 continental-arc zircons. Together, these data support interpretation of the *ca.* 230–250 Ma  
708 zircon population as derived from a juvenile continental-arc system along the eastern  
709 Gondwana margin. They do not distinguish volcanic from plutonic arc sources, but the short  
710 crystallisation-to-deposition age gaps provide the clearest evidence for rapid transfer of young  
711 detritus into the basin.

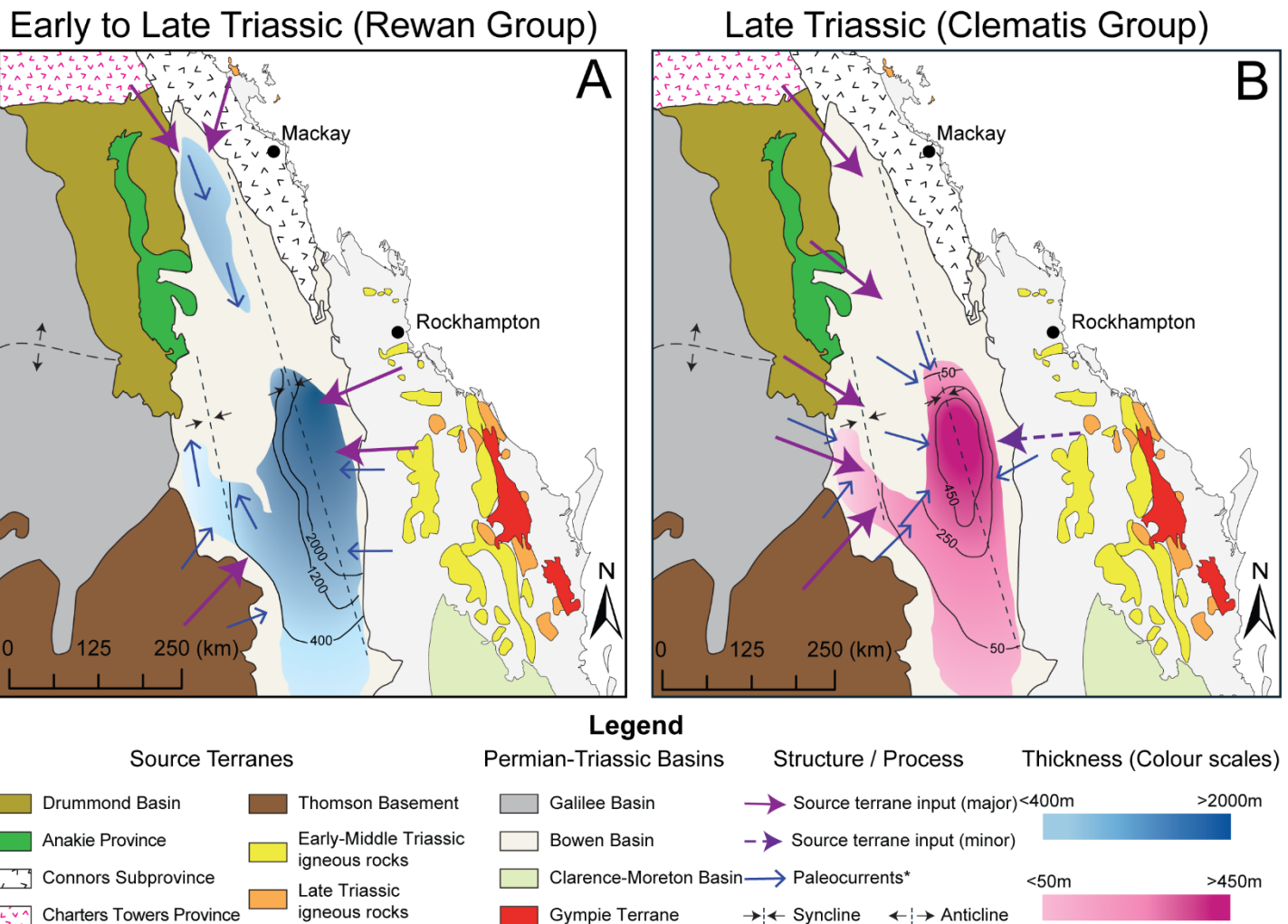
712           The structural framework provides additional context for these provenance trends  
713 (Danis et al., 2012; Babaahmadi et al., 2017; Rosenbaum et al., 2025; Scipione et al., 2026).  
714 Chronostratigraphic constraints indicate earlier and more continuous Triassic accumulation in

715 the Taroom Trough than in the Denison Trough, with a longer interval of non-deposition and/or  
716 erosion in the backbulge (Scipione et al., 2026). Such partitioning is expected in a retroarc  
717 foreland basin where flexural subsidence and intrabasinal structures focus accommodation in  
718 some depocentres while other areas experience bypass or condensation (Korsch, Totterdell,  
719 Fomin, et al., 2009). Despite this segmentation, most Rewan Group samples retain similar age  
720 mixtures across sampled depocentres, implying basin-scale dispersal of arc-derived detritus  
721 during this stage. The offset position of BP1-24-02 suggests local variation in sediment mixing  
722 within the Taroom Trough.

723         The Clematis Group shift is strongest in the Taroom Trough, where older Palaeozoic  
724 components become more prominent and short-lag Triassic input declines. One mechanism is  
725 deformation-driven drainage reorganisation and inversion, which can expose older successions  
726 to erosion, alter gradients, and reroute sediment pathways (Korsch, Totterdell, Cathro, et al.,  
727 2009). Triassic unconformities and changes in basin fill indicate that provenance shifts may  
728 reflect changes in sediment routing and recycling, rather than just a change in source (Brakel  
729 et al., 2009). Reduced accommodation and uplift of intrabasinal highs and backbulge areas can  
730 expose older basin fill to erosion, increase recycling, and dilute the arc-derived signal. The  
731 Clematis Group signal in the Taroom Trough is consistent with this mechanism and with  
732 increased continental-interior input during later Triassic basin evolution.

733         These competing explanations can be tested by sampling additional depocentres: basin-  
734 wide reduction in arc supply versus local rerouting and recycling. If the arc supply decreased  
735 across the whole basin, the Clematis Group spectra should show a similar drop in the Early  
736 Triassic population everywhere. If the change reflects rerouting and recycling, the magnitude  
737 of the shift should vary with structural position and with proximity to unconformities and  
738 inversion features (Babaahmadi et al., 2021; Korsch, Totterdell, Fomin, et al., 2009; Sliwa et

739 al., 2018). Further discrimination would benefit from additional provenance tracers, such as  
 740 zircon Hf isotopes and trace-element chemistry.



741 **Figure 10.** Maps show inferred sediment-transport pathways, potential source terranes, and  
 742 isopach (thickness) trends for (A) the Rewan Group and (B) the Clematis Group. Blue arrows  
 743 show compiled palaeocurrent directions. Purple arrows show interpreted source-terrain  
 744 inputs; solid arrows denote major inputs and dashed arrows denote minor inputs. Thickness  
 745 contours highlight the main depocentres. Potential source regions include the Thomson  
 746 Basement, Drummond Basin, Anakie Province, Charters Towers Province, and Connors  
 747 Subprovince. Palaeocurrent data are compiled from Jensen (1975), Kassan (1994), and Grech  
 748 (2001).

749  
 750 **5.4 Regional comparison and basin-to-basin connectivity**

751 Inter-basin comparison of Triassic detrital zircon age distributions provides an  
 752 empirical test of provenance similarity when evaluated against stratigraphic and sediment-  
 753 transport constraints. Age spectra are compared using KDEs and similarity is evaluated using  
 754 MDS of Wasserstein-2 distances (Figures 8, 9B). The polygons in Figure 9B outline

755 interpretive arc-dominated, mixed, and craton-dominated fields and are used as summaries of  
756 regional similarity structure rather than exact matches.

757         The inferred arc-dominated field contains spectra dominated by Permian–Triassic and  
758 Carboniferous components and captures the Rewan Group-like signal defined within the  
759 Bowen Basin (Figures 6C–D, 8, 9B). Many Gympie Terrane samples and the Bandanna  
760 Formation plot in this field, indicating access to a similar zircon-producing source spectrum  
761 (Li et al., 2015).

762         The inferred mixed and craton-dominated fields are older-weighted than the arc-  
763 dominated field. The Clematis Group sample from the Taroom Trough plots with older-  
764 weighted Galilee Basin Triassic samples, including the Warang Sandstone and Porcupine  
765 Gorge Formation, consistent with reduced young arc input and greater contributions from older  
766 sources (Figures 8, 9B). Todd et al. (2022) place the Porcupine Gorge Formation and Warang  
767 Sandstone broadly within the same Middle–Late Triassic interval as Clematis Group  
768 deposition, within the uncertainty of MDA-based correlation. CT-24-01 is more intermediate  
769 and retains a minor Permian–Triassic peak, although its spectrum is dominated by  
770 Carboniferous ages (Figure 6A).

771         Moolayember Formation reference spectra plot within the arc-dominated field and  
772 show renewed prevalence of younger zircon modes, but stratigraphic uncertainty means that  
773 comparison remains supportive rather than definitive (Figures 8, 9B). Used this way, the  
774 regional comparison helps distinguish shared source access from integrated routing pathways  
775 when similarity patterns are evaluated against basin architecture and palaeocurrent  
776 constraints.

777

## 778 **5.5 Implications for provenance interpretations in other basins**

779 Source-to-sink studies treat the sedimentary system as a connected network linking  
780 source, transfer, and sink (Castelltort et al., 2023; Mason et al., 2022; Romans et al., 2016). In  
781 deep-time settings, provenance data help test whether stratigraphic change reflects rerouting,  
782 recycling, storage, or differential preservation. In the Bowen Basin, the Rewan Group–  
783 Clematis Group transition records such a signal through shifts in detrital zircon spectra,  
784 maximum depositional ages, QFL petrography, and stratal architecture. These changes support  
785 a routing shift, but they do not isolate a single driver or quantify sediment flux through the full  
786 source-to-sink system. Within the Hunter–Bowen Orogeny, a subduction-related convergent-  
787 margin system along eastern Gondwana, this framework shows that combining detrital-zircon  
788 data, petrography, palaeocurrents, and stratigraphy can be used to test changes in sediment  
789 routing across connected basin settings. At a regional scale, this approach helps evaluate  
790 provenance and basin reorganisation from the arc-proximal Gympie Terrane, through the  
791 retroarc foreland Bowen Basin, to the cratonward Galilee Basin.

792 Sorting and recycling remain viable alternatives because both can modify zircon spectra  
793 without requiring a new source terrane. Hydraulic sorting can bias the youngest part of the  
794 zircon spectrum, so it is treated as a possible secondary control. Sorting alone, however, is  
795 unlikely to explain the Clematis Group signal, which also includes stronger older Palaeozoic  
796 modes, more quartzose petrography, and longer crystallisation-to-deposition age gaps (Carraro  
797 et al., 2024; DeGraaff-Surplless et al., 2003; Sylvester et al., 2022). A real change in sediment  
798 supply is therefore preferred, with sorting and sampling bias acting as subordinate modifiers.

799 Signal preservation depends on buffering, delay, and overprinting during transfer and  
800 deposition, and on whether autogenic variability obscures the primary pattern (Mason et al.,  
801 2022; Romans et al., 2016). Robust interpretation therefore requires enough samples and  
802 sufficient chronostratigraphic control to distinguish temporal change from spatial mixing.

803 Multi-cycle recycling, long transport paths, and along-strike mixing can time-average zircon  
804 populations and reduce compositional contrasts, while zircon fertility and lithological targeting  
805 can bias spectra towards zircon-rich sources (Dickinson & Gehrels, 2009).

806 A practical approach is to treat provenance interpretations as testable hypotheses and  
807 evaluate them with a multi-proxy dataset that integrates detrital zircon, QFL petrography,  
808 palaeocurrent data, and stratigraphic architecture (Tucker et al., 2016). Inter-basin comparisons  
809 should use consistent filtering and distance metrics computed from empirical cumulative age  
810 distributions. A Wasserstein-2 dissimilarity matrix can then be used to visualise similarity  
811 structure (Lipp & Vermeesch, 2022; Vermeesch, 2018). Sampling should be densest across key  
812 stratigraphic boundaries and along depositional strike, where routing change and mixing are  
813 most likely to vary. Distance-based results should be reported with grain counts and checked  
814 for sensitivity to sample size. Recycling-dominated intervals may show broader spectra and  
815 longer minimum crystallisation-to-deposition age gaps when MDAs are used as depositional  
816 constraints (Cawood et al., 2012). Time-equivalent units should converge in similarity space  
817 where correlation and transport constraints support a shared routing network. Similarity alone  
818 does not demonstrate sediment transfer.

819

## 820 **Conclusion**

821 This study tested how Triassic provenance and sediment routing changed through time  
822 in the northern Bowen Basin and how those changes relate to adjacent basins and terranes in  
823 eastern Australia.

824 The results define two contrasting provenance states. Rewan Group sandstones share  
825 similar age spectra and occupy the same part of ordination space, indicating a broadly coherent  
826 provenance signal across the sampled structural domains. Short minimum lag times and  
827 feldspar-poor, lithic-rich petrography are consistent with rapid delivery of margin-derived

828 sediment. By contrast, Clematis Group sandstones, especially in the Taroom Trough, show  
829 reduced 220–285 Ma input, more grains older than 400 Ma, and more quartzose petrography.  
830 Together with published palaeocurrents, this pattern indicates reduced east-fed arc supply and  
831 greater cratonward input and/or recycling during Clematis Group deposition.

832 Regional comparisons support that interpretation. Rewan Group spectra resemble the  
833 Bandanna Formation and Gympie Terrane units, whereas Clematis Group spectra are closer to  
834 the Warang Sandstone and Porcupine Gorge Formation. Moolayember Formation reference  
835 spectra shift back towards a Rewan Group-like signature, although that comparison remains  
836 stratigraphically uncertain.

837 Overall, provenance and sediment routing in the northern Bowen Basin changed from  
838 a relatively coherent margin-derived Rewan Group system to a more mixed Clematis Group  
839 system with stronger cratonward and/or recycled input. The main contribution of this study is  
840 to define that shift using an integrated dataset of detrital zircon ages, sandstone petrography,  
841 and palaeocurrent context, and to place it in a regional comparative framework. It therefore  
842 provides a practical basis for testing how provenance-change signals are expressed and  
843 modified in retroarc basin systems.

844

## 845 **Acknowledgements**

846 We gratefully acknowledge the Geological Survey of Queensland and the team at  
847 Zillmere for providing access to the Drake NS27, Taroom 14, Rewan 1 and Theodore NS150.  
848 We also acknowledge the use of facilities and technical support from the Queensland Core  
849 Library (GSQ, Zillmere). We also thank Santos and Mel Wilkinson for permission to sample  
850 the Brumby Plains 1 core, and the landholders at Duckworth Creek, Oaky Creek and Early  
851 Storms Creek for access to outcrop localities. We also thank the Department of the  
852 Environment, Tourism, Science, and Innovation for access to “The Crater” and Mt. Round in

853 the Seracold State Forest. We respectfully acknowledge the Traditional Owners past, present  
854 and emerging of the Country on which this work was conducted, including Bindal,  
855 Wulgurukaba, Bidjara, Gayiri, Gabalara, Gangulu and Biri Country.

856 We are thankful to Huiqing Huang and the AAC staff for their guidance and training  
857 with the LA-ICP-MS system and data reduction workflows. M.S. is grateful to the Team of  
858 Dreams for insightful tips and discussions on Triassic stratigraphy.

859

### 860 **Funding**

861 This work was funded by the James Cook University's College of Science and Engineering  
862 Research Fund.

863

### 864 **Conflict of interest**

865 The authors declare that they have no known competing financial interests or personal  
866 relationships that could have appeared to influence the work reported in this paper.

867

### 868 **Data availability statement**

869 The data supporting this study are included in the article and its supplementary material  
870 (Supplementary Dataset S1, S2 and S3). Additional information is available from the  
871 corresponding author on reasonable request.

872

### 873 **References**

874 Adams, C.J., Campbell, H.J., Korsch, R.J. & Griffin, W.L. (2022) Detrital zircons in Triassic–  
875 Cretaceous sandstones, Clarence-Moreton Basin, eastern Australia: speculations upon  
876 Australia and Zealandia provenances. *Australian Journal of Earth Sciences*, 69(7), 909–  
877 928. <https://doi.org/10.1080/08120099.2022.2070277>.

878 Andrade, C., Sobczak, K., Vasconcelos, P., Holl, H.G., Hurter, S. & Allen, C. (2023) U-Pb  
879 detrital zircon geochronology of the Middle to Upper Jurassic strata in the Surat Basin:  
880 New insights into provenance, paleogeography, and source-sink processes in eastern

- 881 Australia. *Marine and Petroleum Geology*, 149, 106122.  
882 <https://doi.org/10.1016/J.MARPETGEO.2023.106122>.
- 883 Asmussen, P. (2020) *INSIGHTS FROM THE DEVONIAN ADAVALE BASIN ON THE*  
884 *TECTONIC HISTORY OF THE THOMSON OROGEN*.
- 885 Asmussen, P., Gust, D.A., Bryan, S.E., Purdy, D., Murphy, D. & Allen, C.M. (2023)  
886 Multimethod provenance analysis using detrital zircon and rutile U-Pb geochronology  
887 across Devonian basin systems in the Tasmanides of eastern Australia. *Gondwana*  
888 *Research*, 118, 174–191. <https://doi.org/10.1016/J.GR.2023.03.004>.
- 889 Ayaz, S.A., Rodrigues, S., Golding, S.D. & Esterle, J.S. (2016) Compositional variation and  
890 palaeoenvironment of the volcanolithic Fort Cooper Coal Measures, Bowen Basin,  
891 Australia. *International Journal of Coal Geology*, 166, 36–46.  
892 <https://doi.org/10.1016/j.coal.2016.04.007>.
- 893 Babaahmadi, A., Brooks, P. & Grant, M. (2021) Post-orogenic structural style and  
894 reactivation in the northern Bowen Basin, eastern Australia. *Australian Journal of Earth*  
895 *Sciences*, 68(2), 188–203. <https://doi.org/10.1080/08120099.2020.1767206>.
- 896 Babaahmadi, A., Sliwa, R., Esterle, J. & Rosenbaum, G. (2017) The development of a  
897 Triassic fold-thrust belt in a synclinal depositional system, Bowen Basin (eastern  
898 Australia). *Tectonics*, 36(1), 51–77. <https://doi.org/10.1002/2016TC004297>.
- 899 Baker, J.C. (1997) Green ferric clay in non-marine sandstones of the Rewan Group, southern  
900 Bowen Basin, eastern Australia. *Clay Minerals*, 32(4), 499–506.
- 901 Bashari, A. (2000) Petrography and clay mineralogy of volcanoclastic sandstones in the  
902 Triassic Rewan Group, Bowen Basin, Australia. *Petroleum Geoscience*, 6(2), 151–163.  
903 <https://doi.org/10.1144/petgeo.6.2.151>.
- 904 Brakel, A.T., Totterdell, J.M., Wells, A.T. & Nicoll, M.G. (2009) Sequence stratigraphy and  
905 fill history of the Bowen Basin, Queensland. *Australian Journal of Earth Sciences*,  
906 56(3), 401–432. <https://doi.org/10.1080/08120090802698711>.
- 907 Campbell, M.J., Hoy, D., Rosenbaum, G., Fielding, C. & Allen, C.M. (2022) The Onset of  
908 Gondwanide Orogeny in Eastern Australia: Insight From the Provenance of Syn-  
909 Orogenic Strata in the New England Orogen (Australia). *Tectonics*, 41(2).  
910 <https://doi.org/10.1029/2021TC006940>.
- 911 Campbell, M.J., Shaanan, U. & Verdel, C. (2017) Fold-interference patterns in the Bowen  
912 Basin, northeastern Australia. *Australian Journal of Earth Sciences*, 64(5), 577–585.  
913 <https://doi.org/10.1080/08120099.2017.1334704>.
- 914 Carraro, D., Gaynor, S.P., Ventra, D., Ulyanov, A. & Moscariello, A. (2024) Testing the  
915 fidelity of zircon as a provenance indicator in fluvial-fan successions: An example from  
916 the Palaeogene Colton Formation, Central Utah, USA. *Depositional Record*.  
917 <https://doi.org/10.1002/dep2.316>.

- 918 Castellort, S., Fillon, C., Lasseur, É., Ortiz, A., Robin, C., Guillocheau, F., Tremblin, M.,  
919 Bessin, P., Guerit, L., Dekoninck, A., Allanic, C., Gautheron, C., Barbarand, J., Loget,  
920 N., Uzel, J., Yans, J., Briais, J., Al-Reda, M., Baby, G., François, T., Roig, J.-Y. &  
921 Calassou, S. (2023) The Source-to-Sink Vade-mecum: History, Concepts and Tools |  
922 Vade-mecum de l'approche Source-To-Sink: Histoire, Concepts et Outils. *The Source-*  
923 *to-Sink Vade-Mecum: History, Concepts and Tools | Vade-Mecum de l'approche Source-*  
924 *To-Sink: Histoire, Concepts et Outils*. <https://doi.org/10.2110/SEPMCSP.16>.
- 925 Cawood, P.A., Hawkesworth, C.J. & Dhuime, B. (2012) Detrital zircon record and tectonic  
926 setting. *Geology*, 40(10), 875–878. <https://doi.org/10.1130/G32945.1>.
- 927 Collins, W.J. (1991) A reassessment of the 'Hunter-Bowen Orogeny': Tectonic implications  
928 for the southern New England Fold Belt. *Australian Journal of Earth Sciences*, 38(4),  
929 409–423. <https://doi.org/10.1080/08120099108727981>.
- 930 Coutts, D.S., Matthews, W.A. & Hubbard, S.M. (2019) Assessment of widely used methods  
931 to derive depositional ages from detrital zircon populations. *Geoscience Frontiers*,  
932 10(4), 1421–1435. <https://doi.org/10.1016/j.gsf.2018.11.002>.
- 933 Danis, C., O'Neill, C. & Lackie, M. (2012) Building 3D geological knowledge through  
934 regional scale gravity modelling for the Bowen Basin. *Exploration Geophysics*. pp. 8–  
935 25. <https://doi.org/10.1071/EG11028>.
- 936 DeCelles, P.G. & Burden, E.T. (1992) Non-marine sedimentation in the overfilled part of the  
937 jurassic-cretaceous Cordilleran foreland basin: Morrison and Cloverly Formations,  
938 central Wyoming, USA. *Basin Research*, 4(3–4), 291–314.  
939 <https://doi.org/10.1111/j.1365-2117.1992.tb00050.x>.
- 940 DeGraaff-Surpless, K., Mahoney, J.B., Wooden, J.L. & McWilliams, M.O. (2003) Lithofacies  
941 control in detrital zircon provenance studies: Insights from the Cretaceous Methow  
942 basin, southern Canadian Cordillera. *Geological Society of America Bulletin*, 115(8),  
943 899–915. <https://doi.org/10.1130/B25267.1>.
- 944 Dickinson, W.R. & Gehrels, G.E. (2009) Use of U–Pb ages of detrital zircons to infer  
945 maximum depositional ages of strata: A test against a Colorado Plateau Mesozoic  
946 database. *Earth and Planetary Science Letters*, 288(1–2), 115–125.  
947 <https://doi.org/10.1016/J.EPSL.2009.09.013>.
- 948 Dickinson, W.R. & Suczek, C. (1979) Plate Tectonics and Sandstone Compositions. *AAPG*  
949 *Bulletin*, 63(12), 2164–2182. [https://doi.org/10.1306/2F9188FB-16CE-11D7-](https://doi.org/10.1306/2F9188FB-16CE-11D7-8645000102C1865D)  
950 [8645000102C1865D](https://doi.org/10.1306/2F9188FB-16CE-11D7-8645000102C1865D).
- 951 Dutta, P.K. & Wheat, R.W. (1993) Climatic and tectonic control on sandstone composition in  
952 the Permo-Triassic Sydney foreland basin, eastern Australia. *Special Paper of the*  
953 *Geological Society of America*, 284, 187–202. <https://doi.org/10.1130/SPE284-p187>.
- 954 Exon, N.F. (1976) *Geology of the Surat Basin in Queensland*. Australian Government Pub.  
955 Service.

- 956 Fielding, C.R., Frank, T.D., Savatic, K., Mays, C., McLoughlin, S., Vajda, V. & Nicoll, R.S.  
957 (2022) Environmental change in the late Permian of Queensland, NE Australia: The  
958 warmup to the end-Permian Extinction. *Palaeogeography, Palaeoclimatology,*  
959 *Palaeoecology*, 594. <https://doi.org/10.1016/j.palaeo.2022.110936>.
- 960 Fielding, C.R., Stephens, C.J. & Holcombe, R.J. (1997) *Permian stratigraphy and*  
961 *palaeogeography of the eastern Bowen Basin, Gogango Overfolded Zone and*  
962 *Strathmuir Synclinorium in the Rockhampton-Mackay region, central Queensland*.
- 963 Foley, E.K., Baty, M., Knutsen, E.M., Lignum, J.S. & Roberts, E.M. (2020) Jurassic - Early  
964 Cretaceous paleogeography and paleoenvironments of the north-eastern margin of  
965 Gondwana: Insights from the Carpentaria Basin, Australia. *Gondwana Research*, 88,  
966 126–149. <https://doi.org/10.1016/j.gr.2020.07.003>.
- 967 Foley, E.K., Henderson, R.A., Roberts, E.M., Kemp, A.I.S., Todd, C.N., Knutsen, E.M.,  
968 Fisher, C., Wainman, C.C. & Spandler, C. (2021) Jurassic Arc: Reconstructing the Lost  
969 World of eastern Gondwana. *Geology*, 49(11), 1391–1396.  
970 <https://doi.org/10.1130/G49328.1>.
- 971 Garzanti, E. (2016) From static to dynamic provenance analysis—Sedimentary petrology  
972 upgraded. *Sedimentary Geology*, 336, 3–13.  
973 <https://doi.org/10.1016/J.SEDGEO.2015.07.010>.
- 974 Garzanti, E. (2019) Petrographic classification of sand and sandstone. *Earth-Science Reviews*.  
975 Elsevier B.V., pp. 545–563. <https://doi.org/10.1016/j.earscirev.2018.12.014>.
- 976 Glen, R.A. (2005) The Tasmanides of eastern Australia. *Geological Society Special*  
977 *Publication*. pp. 23–96. <https://doi.org/10.1144/GSL.SP.2005.246.01.02>.
- 978 Gómez, R., Lothari, L., Tunik, M. & Casadio, S. (2019) Onset of foreland basin deposition in  
979 the Neuquén Basin (34°-35°S): New data from sedimentary petrology and U–Pb dating  
980 of detrital zircons from the Upper Cretaceous non-marine deposits. *Journal of South*  
981 *American Earth Sciences*, 95(2), 102257. <https://doi.org/10.1016/j.jsames.2019.102257>.
- 982 Grech, P. V (2001) *Sedimentology and sequence stratigraphy of the Early Triassic Rewan*  
983 *Group, Bowen Basin* (Doctoral dissertation). The University of Adelaide.
- 984 Green, P.M., Carmichael, D.C., Brain, T.J., Murray, C.G., McKellar, J., Beeston, J.W. & Gray,  
985 A.R.G. (1997) Lithostratigraphic units in the Bowen and Surat Basins, Queensland. *The*  
986 *Surat and Bowen Basins, South-East Queensland*, 41–108.
- 987 Henderson, R.A. & Fergusson, C.L. (2019) Growth and provenance of a Paleozoic  
988 subduction complex in the Broken River Province, Mossman Orogen: evidence from  
989 detrital zircon ages. *Australian Journal of Earth Sciences*, 66(5), 607–624.  
990 <https://doi.org/10.1080/08120099.2019.1572033>.
- 991 Hoy, D. (2020) *The Hunter-Bowen Orogeny in eastern Australia*.

- 992 Hoy, D., Rosenbaum, G., Mortimer, N. & Shaanan, U. (2018) Hunter–Bowen deformation in  
993 South Percy Island, northeastern Australia. *Australian Journal of Earth Sciences*, 65(2),  
994 175–190. <https://doi.org/10.1080/08120099.2018.1419506>.
- 995 Ingersoll, R., Bullard, T., Ford, R.L., Grimm, J.P., Pickle, J.D. & Sares, S.W. (1984) The  
996 effect of grain size on detrital modes: a test of the Gazzi- Dickinson point-counting  
997 method ( Holocene, sand, New Mexico, USA). *Journal of Sedimentary Petrology*, 54,  
998 103–116.
- 999 Jell, P.A. (2013) *Geology of Queensland*. Geological Survey of Queensland.
- 1000 Jensen, A.R. (1975) *Permo-Triassic stratigraphy and sedimentation in the Bowen Basin,*  
1001 *Queensland*. Canberra.
- 1002 Jessop, K., Daczko, N.R. & Piazzolo, S. (2019) Tectonic cycles of the New England Orogen,  
1003 eastern Australia: A Review. *Australian Journal of Earth Sciences*. Taylor and Francis  
1004 Ltd., pp. 459–496. <https://doi.org/10.1080/08120099.2018.1548378>.
- 1005 Kassan, J. (1994) *Basin analysis of the Triassic succession, Bowen Basin, Queensland*. The  
1006 University of Queensland. <https://doi.org/10.14264/293525>.
- 1007 Korsch, R.J., Totterdell, J.M., Cathro, D.L. & Nicoll, M.G. (2009) Early Permian East  
1008 Australian Rift System. *Australian Journal of Earth Sciences*, 56(3), 381–400.  
1009 <https://doi.org/10.1080/08120090802698703>.
- 1010 Korsch, R.J., Totterdell, J.M., Fomin, T. & Nicoll, M.G. (2009) Contractional structures and  
1011 deformational events in the Bowen, Gunnedah and Surat Basins, eastern Australia.  
1012 *Australian Journal of Earth Sciences*, 56(3), 477–499.  
1013 <https://doi.org/10.1080/08120090802698745>.
- 1014 Lang, S.C., Grech, P., Root, R., Hill, A. & Harrison, D. (2001) THE APPLICATION OF  
1015 SEQUENCE STRATIGRAPHY TO EXPLORATION AND RESERVOIR  
1016 DEVELOPMENT IN THE COOPER-EROMANGA-BOWEN-SURAT BASIN  
1017 SYSTEM. *The APPEA Journal*, 41(1), 223. <https://doi.org/10.1071/aj00011>.
- 1018 Li, P., Rosenbaum, G. & Donchak, P.J.T. (2012) Structural evolution of the Texas Orocline,  
1019 eastern Australia. *Gondwana Research*, 22(1), 279–289.  
1020 <https://doi.org/10.1016/j.gr.2011.09.009>.
- 1021 Li, P., Rosenbaum, G., Yang, J.H. & Hoy, D. (2015) Australian-derived detrital zircons in the  
1022 Permian-Triassic Gympie terrane (eastern Australia): Evidence for an autochthonous  
1023 origin. *Tectonics*, 34(5), 858–874. <https://doi.org/10.1002/2015TC003829>.
- 1024 Li, P.F., Rosenbaum, G. & Rubatto, D. (2012) Triassic asymmetric subduction rollback in the  
1025 southern New England Orogen (eastern Australia): the end of the Hunter-Bowen  
1026 Orogeny. *Australian Journal of Earth Sciences*, 59(6), 965–981.  
1027 <https://doi.org/10.1080/08120099.2012.696556>.

- 1028 Lipp, A. & Vermeesch, P. (2022) Short communication: The Wasserstein distance as a  
1029 dissimilarity metric for comparing detrital age spectra and other geological distributions.  
1030 *Geochronology*, 5(1), 263–270. <https://doi.org/10.5194/gchron-5-263-2023>.
- 1031 Maravelis, A.G., Offler, R., Botziolis, C., Pantopoulos, G., Scott, A., Landenberger, B. &  
1032 Collins, W.J. (2023) Provenance of a Late Permian retroarc foreland basin along the  
1033 eastern Gondwanan margin: northern Sydney Basin, eastern Australia. *Geological*  
1034 *Magazine*, 160(8), 1535–1555. <https://doi.org/10.1017/S0016756823000535>.
- 1035 Mason, C.C., Romans, B.W., Patterson, M.O., Stockli, D.F. & Fildani, A. (2022) Cycles of  
1036 Andean mountain building archived in the Amazon Fan. *Nature Communications* 2022  
1037 13:1, 13(1), 6983-. <https://doi.org/10.1038/s41467-022-34561-6>.
- 1038 McKellar, J.L., Ayaz, A., Laurie Geoscience Australia, J.R., Nicoll, R., McKellar, J., Areeba  
1039 Ayaz, S., Laurie, J., Esterle, J., Crowley, J., Wood, G. & Bodorkos, S. (2015) *CA-*  
1040 *IDTIMS dating of tuffs, calibration of palynostratigraphy and stratigraphy of the Bowen*  
1041 *and Galilee basins*.
- 1042 Michaelsen, P. & Henderson, R.A. (2000) Sandstone petrofacies expressions of multiphase  
1043 basinal tectonics and arc magmatism: Permian-Triassic north Bowen Basin, Australia.  
1044 *Sedimentary Geology*, 136(1–2), 113–136. [https://doi.org/10.1016/S0037-](https://doi.org/10.1016/S0037-0738(00)00090-7)  
1045 [0738\(00\)00090-7](https://doi.org/10.1016/S0037-0738(00)00090-7).
- 1046 Naher, J., Fielding, C.R. & Martin, M.A. (2025) Misleading Basin Margins—Analysis of the  
1047 Upper Permian Succession in the Retroarc Foreland Bowen Basin of Northeast  
1048 Australia. *Basin Research*, 37(3), e70033.  
1049 <https://doi.org/10.1111/BRE.70033>;REQUESTEDJOURNAL:JOURNAL:13652117;W  
1050 GROUP:STRING:PUBLICATION.
- 1051 Paton, C., Hellstrom, J., Paul, B., Woodhead, J. & Hergt, J. (2011) Iolite: Freeware for the  
1052 visualisation and processing of mass spectrometric data. *Journal of Analytical Atomic*  
1053 *Spectrometry*, 26(12), 2508–2518. <https://doi.org/10.1039/C1JA10172B>.
- 1054 Phillips, G., Landenberger, B. & Belousova, E.A. (2011) Building the New England  
1055 Batholith, eastern Australia—Linking granite petrogenesis with geodynamic setting  
1056 using Hf isotopes in zircon. *Lithos*, 122(1–2), 1–12.  
1057 <https://doi.org/10.1016/J.LITHOS.2010.11.005>.
- 1058 Phillips, L.J., Edwards, S.A., Bianchi, V. & Esterle, J.S. (2017) Paleo-environmental  
1059 reconstruction of Lopingian (upper Permian) sediments in the Galilee Basin,  
1060 Queensland, Australia. *Australian Journal of Earth Sciences*, 64(5), 587–609.  
1061 <https://doi.org/10.1080/08120099.2017.1338618>.
- 1062 Phillips, L.J., Verdel, C., Allen, C.M. & Esterle, J.S. (2018) Detrital zircon U–Pb  
1063 geochronology of Permian strata in the Galilee Basin, Queensland, Australia. *Australian*  
1064 *Journal of Earth Sciences*, 65(4), 465–481.  
1065 <https://doi.org/10.1080/08120099.2018.1467261>.

- 1066 Purdy, D.J., Cross, A.J., Brown, D.D., Carr, P.A. & Armstrong, R.A. (2016) New constraints  
1067 on the origin and evolution of the Thomson Orogen and links with central Australia from  
1068 isotopic studies of detrital zircons. *Gondwana Research*, 39, 41–56.  
1069 <https://doi.org/10.1016/J.GR.2016.06.010>.
- 1070 Romans, B.W., Castelltort, S., Covault, J.A., Fildani, A. & Walsh, J.P. (2016) Environmental  
1071 signal propagation in sedimentary systems across timescales. *Earth-Science Reviews*,  
1072 153(6), 7–29. <https://doi.org/10.1016/j.earscirev.2015.07.012>.
- 1073 Rosenbaum, G. (2026) The plate tectonic setting of mineral deposits in the New England  
1074 Orogen (Australia). *Earth-Science Reviews*, 276, 105435.  
1075 <https://doi.org/10.1016/j.earscirev.2026.105435>.
- 1076 Rosenbaum, G., Babaahmadi, A., Glorie, S. & Schellart, W.P. (2025) Development of arc  
1077 curvature by asymmetric migration: Evidence from Permian–Triassic granitoids in the  
1078 New England Orogen (eastern Australia). *Earth and Planetary Science Letters*, 653,  
1079 119209. <https://doi.org/10.1016/J.EPSL.2025.119209>.
- 1080 Rosenbaum, G., Slade, A. & Hoy, D. (2020) Sedimentological responses to the Hunter–  
1081 Bowen Orogeny (eastern Australia): evidence from the northern Gympie Terrane.  
1082 *Australian Journal of Earth Sciences*, 67(1), 59–73.  
1083 <https://doi.org/10.1080/08120099.2019.1648317>.
- 1084 Scipione, M., Vaucher, R., Roberts, E., McCoy-West, A.J., Esterle, J., Turner, A. & Knutsen,  
1085 E. (2026) Shifting the Paradigm: Redefining the Chronostratigraphy of the Triassic  
1086 Rewan Group, Bowen Basin, Australia. *Basin Research*, 38(3), e70102.  
1087 <https://doi.org/10.1111/BRE.70102;ISSUE:ISSUE:DOI>.
- 1088 Shaanan, U. & Rosenbaum, G. (2018) Detrital zircons as palaeodrainage indicators: insights  
1089 into southeastern Gondwana from Permian basins in eastern Australia. *Basin Research*,  
1090 30, 36–47. <https://doi.org/10.1111/bre.12204>.
- 1091 Shaanan, U., Rosenbaum, G. & Sihombing, F.M.H. (2018) Continuation of the Ross–  
1092 Delamerian Orogen: insights from eastern Australian detrital-zircon data. *Australian  
1093 Journal of Earth Sciences*, 65(7–8), 1123–1131.  
1094 <https://doi.org/10.1080/08120099.2017.1354916>.
- 1095 Shaw, S.E., Flood, R.H. & Pearson, N.J. (2011) The New England Batholith of eastern  
1096 Australia: Evidence of silicic magma mixing from zircon 176Hf/177Hf ratios. *Lithos*,  
1097 126(1–2), 115–126. <https://doi.org/10.1016/J.LITHOS.2011.06.011>.
- 1098 Siegel, C., Bryan, S.E., Allen, C.M., Gust, D.A. & Purdy, D.J. (2020) Crustal evolution in the  
1099 New England orogen, Australia: Repeated igneous activity and scale of magmatism  
1100 govern the composition and isotopic character of the continental crust. *Journal of  
1101 Petrology*, 61(8). <https://doi.org/10.1093/petrology/egaa078>.

- 1102 Sliwa, R., Babaahmadi, A. & Esterle, J. (2018) *ACARP Project C24032: Structure*  
1103 *Supermodel 2017-Fault Characterisation in Permian to Jurassic Coal Measures For the*  
1104 *Australian Coal Association Research Program (ACARP).*
- 1105 Sobczak, K., La Croix, A.D., Esterle, J., Hayes, P., Holl, H.G., Ciesiolka, R., Crowley, J.L. &  
1106 Allen, C.M. (2022) Geochronology and sediment provenance of the Precipice Sandstone  
1107 and Evergreen Formation in the Surat Basin, Australia: Implications for the  
1108 palaeogeography of eastern Gondwana. *Gondwana Research, 111*, 189–208.  
1109 <https://doi.org/10.1016/j.gr.2022.08.003>.
- 1110 Spampinato, G.P.T., Betts, P.G., Ailleres, L. & Armit, R.J. (2015) Early tectonic evolution of  
1111 the Thomson Orogen in Queensland inferred from constrained magnetic and gravity  
1112 data. *Tectonophysics, 651–652*, 99–120. <https://doi.org/10.1016/J.TECTO.2015.03.016>.
- 1113 Sylvester, P.J., Souders, A.K. & Liu, R. (2022) Significance of U-Pb detrital zircon  
1114 geochronology for mudstone provenance. *Geology, 50*(6), 670–675.  
1115 <https://doi.org/10.1130/G49684.1>.
- 1116 Todd, C. (2020) The sedimentary evolution of Permian to Cretaceous basins in Queensland,  
1117 Australia: insights from lithostratigraphy, U–Pb zircon geochronology, sedimentary  
1118 facies, and provenance analysis. <https://doi.org/10.25903/x1pq%2Dxc37>.
- 1119 Todd, C.N., Roberts, E.M. & Charles, A.J. (2022) A revised Permian–Triassic stratigraphic  
1120 framework for the northeastern Galilee Basin, Queensland, Australia, and definition of a  
1121 new Middle–Upper Triassic sedimentary unit. *Australian Journal of Earth Sciences,*  
1122 *69*(1), 113–134. <https://doi.org/10.1080/08120099.2021.1931962>.
- 1123 Tucker, R.T., Roberts, E.M., Henderson, R.A. & Kemp, A.I.S. (2016) Large igneous province  
1124 or long-lived magmatic arc along the eastern margin of Australia during the Cretaceous?  
1125 Insights from the sedimentary record. *Bulletin of the Geological Society of America,*  
1126 *128*(9–10), 1461–1480. <https://doi.org/10.1130/B31337.1>.
- 1127 Tucker, R.T., Roberts, E.M., Hu, Y., Kemp, A.I.S. & Salisbury, S.W. (2013) Detrital zircon  
1128 age constraints for the Winton Formation, Queensland: Contextualizing Australia’s Late  
1129 Cretaceous dinosaur faunas. *Gondwana Research, 24*(2), 767–779.  
1130 <https://doi.org/10.1016/J.GR.2012.12.009>.
- 1131 Van Heeswijck, A. (2010) Late paleozoic to early Mesozoic deformation in the northeastern  
1132 Galilee Basin, Australia. *Australian Journal of Earth Sciences, 57*(4), 431–451.  
1133 <https://doi.org/10.1080/08120099.2010.481328>.
- 1134 Van Heeswijck, A. (2018) Fluvial sequences and basin development in the northern Galilee  
1135 Basin. *Australian Journal of Earth Sciences, 65*(3), 367–389.  
1136 <https://doi.org/10.1080/08120099.2018.1437772>.
- 1137 Vermeesch, P. (2012) On the visualisation of detrital age distributions. *Chemical Geology,*  
1138 *312–313*, 190–194. <https://doi.org/10.1016/J.CHEMGEO.2012.04.021>.

- 1139 Vermeesch, P. (2018) IsoplotR: A free and open toolbox for geochronology. *Geoscience*  
1140 *Frontiers*, 9(5), 1479–1493. <https://doi.org/10.1016/J.GSF.2018.04.001>.
- 1141 Vermeesch, P. (2021) Maximum depositional age estimation revisited. *Geoscience Frontiers*,  
1142 *12(2)*, 843–850. <https://doi.org/10.1016/J.GSF.2020.08.008>.
- 1143